Original Paper

phys. stat. sol. (a) **202**, No. 7, 1193–1207 (2005) / **DOI** 10.1002/pssa.200460900

Non-destructive, room temperature characterization of wafer-sized III–V semiconductor device structures using contactless electromodulation and wavelength-modulated surface photovoltage spectroscopy

Y. S. Huang[*, 1] and **F. H. Pollak**[2, 3]

[1] Department of Electronic Engineering, National Taiwan University of Science and Technology, Taipei 106, Taiwan
[2] Department of Physics and New York State Center for Advanced Technology in Ultrafast Photonic Materials and Applications, Brooklyn College of the City University of New York, Brooklyn, New York 11210, USA
[3] Semiconductor Characterization Instruments, Inc., 146 Columbia Heights Suite #2, Brooklyn, New York 11201, USA

Received 19 August 2004, revised 20 January 2005, accepted 4 February 2005
Published online 21 March 2005

PACS 42.55.Px, 78.20.Jq, 78.40.Fy, 78.66.Fd, 85.30.Pq, 85.30.Tv

We review the use of the contactless methods of photoreflectance (PR), contactless electroreflectance (CER) and wavelength modulated differential surface photovoltage spectroscopy (DSPS) for the nondestructive, room temperature characterization of a wide variety of wafer-scale III–V semiconductor device structures. Some systems that will be discussed include heterojunction bipolar transistors (including the determination of the built-in fields/doping levels in the emitter and collector regions, alloy composition, and dc current gain factor), pseudomorphic GaAlAs/InGaAs/GaAs high electron mobility transistors (including the determination of the composition, width, and two-dimensional electron gas density in the channel), InGaAsP/InP quantum well edge emitting lasers (including the detection of p-dopant interdiffusion), vertical-cavity surface-emitting lasers (determination of fundamental conduction to heavy-hole excitonic transition and cavity mode).

1 Introduction

In the past two decades there have been considerable advances in semiconductor device fabrication due to thin film growth by techniques such as molecular beam epitaxy (MBE), organo-metallic chemical vapor deposition (OMCVD) and gas phase MBE as well as various processing procedures. Developmental efforts are driving device design toward more compact structures. The trend places ever increasing demands on device parameters and hence evaluation procedures in order to upgrade performance and yield.

The devices produced by modern growth/processing methods can be characterized by a variety of optical, electrical and structural measurements including photoluminescence (PL), electroluminescence (EL), photoluminescence excitation spectroscopy (PLE), absorption spectroscopy, photoconductivity (PC), spectral ellipsometry, modulation spectroscopy, Raman and resonance Raman scattering, resistivity, Hall effect, current–voltage (I–V) and capacitance–voltage (C–V), cyclotron resonance, transmis-

[*] Corresponding author: e-mail: ysh@et.ntust.edu.tw, Phone: +886 2 27376385, Fax: +886 2 27376424

sion electron microscopy (TEM), secondary ion mass spectrometry (SIMS), etc. Many of the methods mentioned above are specialized, destructive and difficult to employ. Also, a number of these techniques generally require cryogenic temperatures.

For applied work, an optical characterization technique should be as simple, inexpensive, compact, rapid and informative as possible. Other valuable aspects are the ability to perform measurements in a contactless manner at (or even above) room temperature on wafer-sized samples. Because of its simplicity and proven ability, modulation spectroscopy (particularly contactless modes) is now a major tool for the study and characterization of bulk/thin film semiconductors [1–5] in addition to semiconductor microstructures (quantum wells (QWs), superlattices, quantum dots, etc.) [1–3] and interfaces (heterojunctions, semiconductor/vacuum, semiconductor/metal) [1–5]. Furthermore, this optical method is also useful for the evaluation of process-induced damage [1–3]. Recent works also have clearly demonstrated its considerable potential and growing importance in the evaluation of important device parameters for structures such as heterojunction bipolar transistors (HBTs) [6–16], pseudomorphic high electron mobility transistors (PHEMTs) [17–27], edge emitting quantum well lasers [28–31], and vertical cavity surface-emitting lasers (VCSELs) [32–39].

Modulation spectroscopy is an analog method for taking the derivative of the optical spectrum (reflectance or transmittance) of a material by modifying in some manner the measurement conditions [1–5]. The basic idea of this optical technique is a very general principle of experimental physics. Instead of measuring the optical reflectance (or transmittance) of the material, the derivative with respect to some parameter is evaluated. This can easily be accomplished by varying some property of the sample or measuring system in a periodic fashion and measuring the corresponding normalized change in the reflectance (transmittance).

The periodic variation of the measurement conditions give rise to sharp, differential-like spectra in the region of interband (intersubband) transitions. Therefore, modulation spectroscopy emphasizes relevant spectral features and suppresses uninteresting background effects. The ability to perform a lineshape fit is one of the great advantages of modulation spectroscopy. Since for the modulated signal the features are localized in photon energy it is possible to account for the lineshapes to yield accurate values of interband (intersubband) transition energies, broadening parameters, Fermi energies, etc. For example, even at 300 K it is possible to determine the energies of spectral features to within a few meV. Because the changes in the optical spectra are typically small, in some cases 1 part in 10^6, phase sensitive detection or some other signal processing procedure is required. Since modulation spectroscopy is a normalized technique not every photon need be collected as long as there are enough to produce a good signal-to-noise ratio. Thus, this experimental method does not have stringent conditions on the morphology of the sample surface.

A particularly useful form of modulation spectroscopy is electromodulation (EM) since it is sensitive to surface/interface electric fields and can be performed in nondestructive modes such as photoreflectance (PR) and contactless electroreflectance (CER) that require no special mounting of the sample. Therefore, these modes can be employed on wafer-sized material without altering the sample [1–4]. The most widely used form of EM is PR.

The sensitivity of EM methods such as PR/CER to surface/interface electric field has proven to be one of its most important properties for device characterization. For sufficiently high built-in electric fields the EM spectrum can display an oscillatory behavior above the band gap called Franz-Keldysh oscillations (FKOs). The period of these FKOs is a direct measure of the relevant built-in electric field [1–5].

Surface photovoltage spectroscopy (SPS) monitors the photoinduced changes in the surface potential caused by photon absorption and charge carrier separation in the bulk, at structure interfaces, and at the outer surface of the sample. In SPS the contact potential difference between the sample and a reference electrode is measured in a capacitive manner by either (a) vibrating the reference electrode (Kelvin probe) or (b) leaving the reference electrode fixed and chopping the incident light. The technique of SPS has been used to study a wide range of phenomenon in semiconductors including bulk/thin films, heterostructures, surfaces/interfaces, and QWs/superlattices [40–43]. However, until the last decade very

little work has been reported on actual device structures. Mishori et al. were able to deduce the p-dopant level and minority carrier lifetime in the base of a GaAlAs/GaAs HBT [44]. Cheng et al. reported a SPS characterization of a GaAlAs/InGaAs/GaAs PHEMT [45]. SPS investigations of a graded index of refraction separate confinement heterostructure (GRINSCH) quantum well laser [46], GaAs/GaAlAs based VCSELs [47–49] and 1.3 μm InGaAlAs/InP VCSELs [50] are reported. Recently Wang et al. [51] and Liang et al. [52] have reported wavelength modulated differential surface photovoltage spectroscopy (DSPS) study of 850 nm GaAs/GaAlAs and 1.3 μm InGaAlAs/InP VCSELs structures, respectively. The results demonstrate considerable potential of DSPS for the nondestructive characterization of VCSEL structures at room temperature.

2 Basic techniques

Shown in Fig. 1 is a schematic drawing of the PR system developed at Brooklyn College [1, 2]. In PR modulation of the built-in electric field is caused by photo-excited electron–hole pairs created by a pump source of ~3–5 mW power of either (a) an internally modulated laser diode or (b) mechanically chopped *dc* laser. The photon energy of the pump beam is generally larger than the lowest energy gap of the material. The modulating frequency is typically ≈200 Hz. The entire data acquisition procedure can be placed under computer control. Multiple scans over a given photon energy range can be programmed until a desired signal-to-noise level has been attained. The computer also can be used for data analysis, such as lineshape fits, and comparison of results with the data base.

In CER, which requires no pump beam, an *ac* modulating voltage (~1 kV at ≈200 Hz) is applied between a front wire grid electrode and a second electrode consisting of a metal plate, which has holes so that a vacuum can be applied to hold the sample in contact with the plate (i.e., vacuum chuck) [1, 4]. These two electrodes are separated by insulating spacers, such that there is a very thin layer (~0.1 mm) of air (or vacuum) between the front surface of the sample and the front electrode. Thus, there is nothing in direct contact with the front surface of the sample. The probe beam is incident through the front wire grid. The absence of the pump beam in CER avoids certain problems encountered in PR such as (a) a PL background in high quality samples and (b) photoexcited carriers which can sometimes alter the measured parameters. Since CER uses no pump beam it can conventially be used to study EM on large band gap materials such as the group III-nitrides [53]. Furthermore with CER it is possible to determine the nature of the band bending (n- or p-type) at surfaces or buried interfaces (using a reference sample) [54].

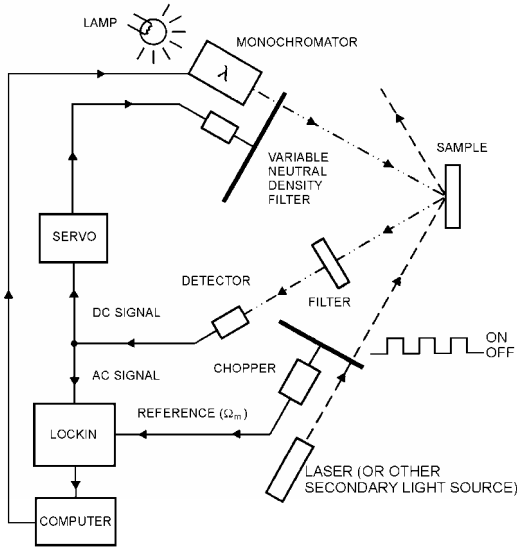

Fig. 1 Schematic representation of the photoreflectance apparatus developed at Brooklyn College.

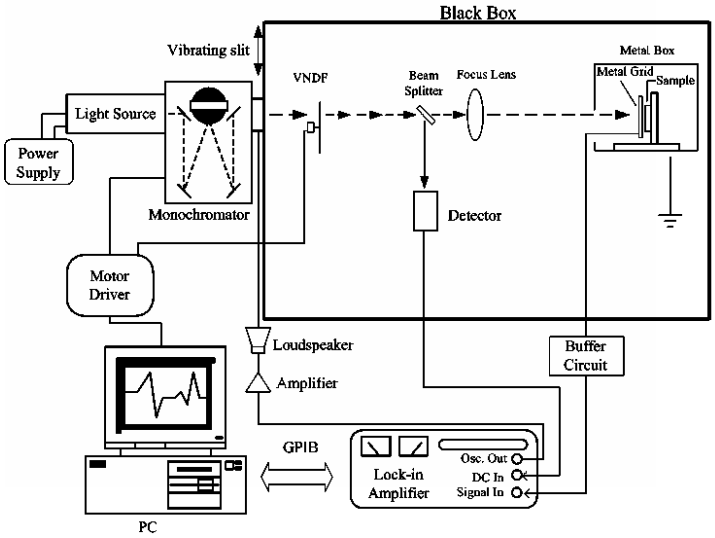

Fig. 2 Schematic diagram of the wavelength modulated surface photovoltage spectroscopy setup.

As mentioned above one of the problems with PR is the PL induced by the pump beam. One of the initial approaches to this problem was front-end compensation (FEC) [55]. FEC uses a properly phase-shifted signal from the reference source that is applied to the lock-in amplifier's (LIA) differential input. The monochromator is first moved to a wavelength where no PR signal would be expected. The LIA is set to a phase angle that maximizes the dominant PL signal and then adds or subtracts 90° to zero the PL so that the remaining signal is PR. Other approaches to the PL problem are the use of a double monochromator [56], tunable dye laser probe beam [57], sweeping PR [58] or differential PR [59].

In DSPS, the derivative-like surface photovoltage is measured between the sample and a reference metal grid electrode in a capacitive manner as a function of the photon energy of the probe beam with a wavelength-modulation technique [51, 52]. Figure 2 shows the schematic diagram of the wavelength modulated DSPS setup. The illumination system consisted of a 150 W quartz-halogen lamp and a grating monochromator equipped with a vibrating exit slit operated by a power amplifier, employing a 2″ loudspeaker as transducer. A beam splitter was placed in the path of the incident light. The intensity of this radiation was monitored by a power meter and was kept constant by a stepping motor connected to a variable neutral density filter, which was also placed in the path of the incident beam. The incident light intensity was maintained at a constant level of ~10^{-4} W/cm^2. The illumination intensity and the amplitude of wavelength modulation were experimentally selected at levels not affecting the measured spectra; typically $\Delta\lambda/\lambda$ was on the order of 10^{-3}. Precautions need to be taken to eliminate the spurious signals from light-intensity modulation. The normalized wavelength-modulated derivative-like photovoltage spectrum on the metal grid was measured with a copper plate as the ground electrode, using a buffer circuit and a lock-in amplifier.

3 Applications

3.1 Heterojunction bipolar transistors

Heterojunction bipolar transistors have been under development for the past two decades due to their advantages for high-speed operation over other semiconductor devices. Development of HBT technology has been hampered by the extreme sensitivity of device performance to small variations in the epitaxial structures, either intentional or unintentional. The general consensus is that the most critical region for determining overall device performance is the base–emitter region. Small differences in the placement of

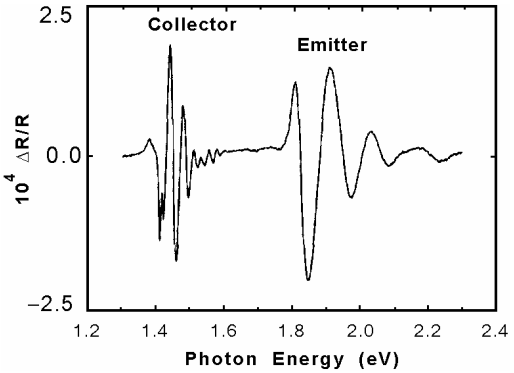

Fig. 3 Photoreflectance spectrum in the region of the direct gaps of GaAs (collector) and GaAlAs (emitter) from a GaAs/GaAlAs HBT at 300 K.

the base–emitter p–n junction relative to the heterojunction can have considerable impact on the characteristics of the device.

It has been shown that PR/CER can be effective tools in the room temperature, production-line qualification of wafer-scale HBT structures such as graded emitter GaAlAs/GaAs [6–10], GaInP/GaAs [11], GaInP/GaInNAs/GaAs [12, 13], InP/InGaAs [14], and InAlAs/InGaAs [15, 16] configurations. The FKOs observed from the collector/base and emitter/base regions can be used to evaluate the built-in electric fields in these regions. Doping densities can be determined by taking into account corrections for the photovoltaic effect. Also the composition of the alloy can be determined. It has been shown both theoretically and experimentally that for the graded emitter GaAlAs/GaAs configuration the observed FKOs from the emitter are due to both space-charge and grading fields. For the GaInP/GaAs system the polarization dependence of the signals from the emitter ([110] and [1$\bar{1}$0] of the incident radiation) have been used to determine the degree of ordering of the alloy. The ordering parameters deduced from the polarization dependence are consistent with TEM measurements.

Shown in Fig. 3 is the PR spectrum at 300 K from the collector (GaAs) and emitter (GaAlAs) regions for an MBE fabricated HBT sample [6] with the following characteristics. The collector contact layer, 6000 Å of n^+-GaAs:Si ($\approx 5 \times 10^{18}$ cm^{-3}), was grown on an undoped liquid encapsulated Czochralski (001) semi-insulating substrate. This was followed by the collector layer of 7000 Å of n^--GaAs:Si ($n^{\text{coll}} \approx 7.5 \times 10^{15}$ cm^{-3}) and 1400 Å of p^+-GaAs:Be base ($p^{\text{base}} \approx 1 \times 10^{19}$ cm^{-3}). The 1800 Å of n-GaAlAs:Si emitter ($n^{\text{emit}} \approx 5 \times 10^{17}$ cm^{-3}) emitter was graded in Al composition at the top and bottom over 300 Å. The n^+-GaAs:Si ($\approx 7 \times 10^{18}$ cm^{-3}) emitter contact layer was about 750 Å thick. The intensities of the pump and probe beams were 600 μW/cm^2 and 100 μW/cm^2, respectively.

The band gap of GaAs is 1.42 eV while the band gap of the GaAlAs portion of the sample is 1.830 eV, which corresponds to an Al composition of 28%. The oscillatory features above the band gaps are the FKO's. The position of the m-th extremum in the FKOs are given by [1, 2]

$$m\pi = \left\{ \frac{4\sqrt{2}}{3q\hbar F} \left[\frac{m_c^* m_{hh}^* (001)}{m_c^* + m_{hh}^*} \right]^{1/2} (E_m - E_0)^{3/2} \right\} + \chi \,, \tag{1}$$

where E_m is the photon energy of the mth extremum, E_0 is the band gap, F is the field, and χ is an arbitrary phase factor, while m_c^* and $m_{hh}^*(001)$ are the effective masses of the electron and heavy hole [along (001)], respectively, in units of the free-electron mass. Therefore, a plot of $(\frac{4}{3}\pi)$ $(E_m - E_0)^{3/2}$ as a function of index number m yields a straight line from which F can be evaluated from Eq. (1). It has been shown that for nonuniform fields, such as the ones that exist in p–n junctions, the FKOs are a measure of the maximum field in the structure.

Using this procedure it was possible to directly evaluate F_{dc} in the collector–base and emitter–base regions, respectively, by this nondestructive optical approach. The most important aspects of Fig. 3 are the FKOs associated with the GaAlAs band gap. From these features it is possible to evaluate F_{dc} in the

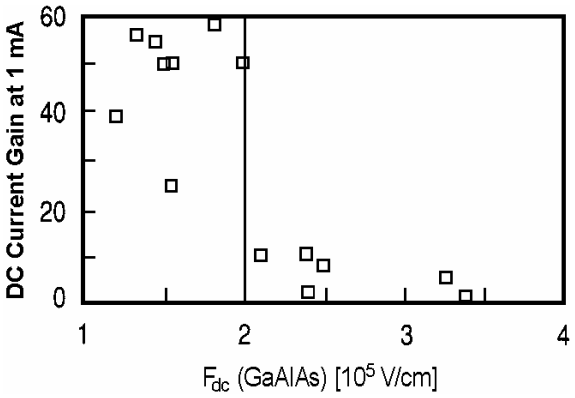

Fig. 4 Current gain at 1 mA as a function of F_{dc} (GaAlAs) for actual GaAs/GaAlAs HBT device fabricated from MBE grown samples.

emitter–base n–p junction. The electric fields as deduced from the GaAlAs FKOs [F_{dc} (GaAlAs)] were compared with actual GaAs/GaAlAs HBT device parameters fabricated from MBE-grown samples. Below electric field values of about 2×10^5 V/cm high current gains were obtained.

Shown in Fig. 4 is F_{dc} (GaAlAs) as a function of dc current gain at 1 mA for a number of MBE grown samples. Note that there is a sudden drop when F_{dc} (GaAlAs) $> 2 \times 10^5$ V/cm. The explanation of this effect is the redistribution of the Be dopant in the p-region in these MBE samples. When the redistribution moves the p–n junction into the emitter, there is an increase in the electric field in this region, i.e. the value of F_{dc} becomes greater. The movement of the Be has been verified by secondary ion mass spectroscopy (SIMS). When the p–n junction and the GaAs/GaAlAs heterojunction are not coincident, carrier recombination occurs, reducing the current and the performance of fabricated HBTs. These observations have made it possible to use PR as a screening technique to eliminate wafers with unwanted characteristics before the costly fabrication step.

The GaInP/GaAs HBT samples of Ref. [11] were fabricated on undoped liquid encapsulated Czochralski (001) semi-insulating GaAs substrates by either OMCVD (sample A) or CBE (sample B) with the following characteristics. On top of the 5000 Å undoped GaAs buffer was grown (a) 3000 Å of n-doped (Si) 5×10^{18} cm^{-3} followed by the (b) collector layer of 4000 Å of n$^-$-GaAs:Si ($n^{coll} \approx 4 \times 10^{16}$ cm^{-3}) and the (c) 500 Å p$^+$-GaAs:C base ($p^{base} \approx 4 \times 10^{19}$ cm^{-3}). The 500 Å n-GaInP:Si emitter had $n^{emit} \approx (4 \pm 1)\ 10^{17}$ cm^{-3} while the n$^+$-GaAs:Si ($\approx 6 \times 10^{18}$ cm^{-3}) emitter contact layer was about 2000 Å thick.

Shown by the dashed lines in Figs. 5(a) and (b) are the 300 K CER spectra of sample A for light with electric field vector $\boldsymbol{E} \| [110]$ and $\boldsymbol{E} \| [1\bar{1}0]$, respectively. The solid lines are least-square fits to a function which contains Lorentzian broadened electro-optic functions, yielding 1.873 ± 0.001 and 1.885 ± 0.001 eV for the GaInP band gaps for [110] and [1$\bar{1}$0] polarizations, respectively, as indicated by the arrows.

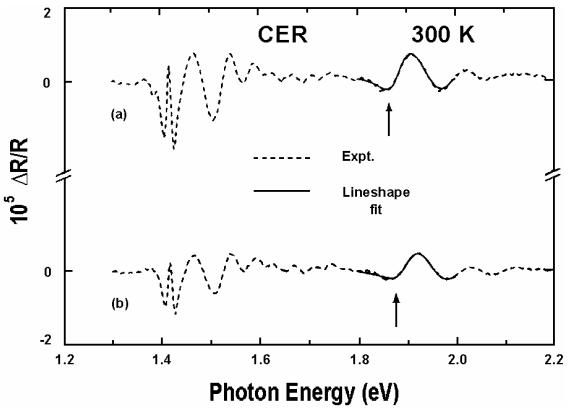

Fig. 5 Room temperature CER spectra (dashed line) of a GaInP/GaAs HBT grown by OMCVD (sample A) for light polarized (a) $\boldsymbol{E} \| [110]$ and (b) $\boldsymbol{E} \| [1\bar{1}0]$. The solid lines are a line-shape fit which yields the energies denoted by arrows.

For sample A the authors obtained F^{coll} = 75 ± 3 kV/cm using m_c^* = 0.067 and m_{hh}^* (001) = 0.34 for GaAs. For GaInP there is some discrepancy concerning both m_c^* and m_{hh}^* (001). One reference [60] reports 0.092 and 0.48, respectively, while another [61] cites 0.118 and 0.66, respectively. The obtained F^{emit} = 160 ± 3 kV/cm and 180 ± 3 kV/cm, respectively. Similar results were obtained for sample B with 1.900 ± 0.001 eV and 1.903 ± 0.001 eV for GaInP band gaps for [110] and [1$\bar{1}$0] polarization, respectively, collector field of 70 ± 3 kV/cm, and emitter fields of either 180 ± 3 kV/cm and 205 ± 3 kV/cm, depending on the above mentioned choice of masses.

The ordering parameters (η) deduced from the differences in the measured band gaps for the two polarizations (0.30 for sample A and 0.09 for sample B) were consistent with transmission electron microscope measurements. The measured electric fields from the emitter and collector regions were compared with a computer simulation of the field profiles using a comprehensive, self-consistent model with the structure parameters listed above, including the influence of the light (i.e. photovoltaic effect). The deduced emitter and collector doping densities were 3×10^{17} cm^{-3} and 4×10^{16} cm^{-3}, respectively, in good agreement with the intended growth conditions.

The n–p–n double-heterojunction bipolar transistor structure GaInP/GaInNAs/GaAs was characterized by Lin et al. [12] using polarized PR spectroscopy. The ordering parameter of the GaInP was deduced from the polarization ([110] and [1$\bar{1}$0]) dependence of the PR signals from the emitter region. The ordering-related piezoelectric field was also found to influence the electric field, as evaluated from the FKOs observed in the GaInP emitter region. The field in the emitter region was found to be ~25 kV/cm smaller than the theoretical value that does not take into account the possible ordering induced screening effect, while the field in the collector region agrees well with the theoretical value. In addition, the GaInNAs band gap was also determined by analyzing the PR spectrum of the base region.

3.2 High electron mobility transistor structures

High electron mobility transistors offer superior transistor noise performance compared to other solid-state amplifiers. HEMTs have gained wide-spread acceptance as the device of choice for the majority of high performance receivers at frequencies up to 100 GHz. They are also proving to be an excellent choice for power amplifiers. One type of HEMT in particular, the pseudomorphic $Ga_{1-y}Al_yAs$/$In_xGa_{1-x}As$/GaAs modulation doped structure, has demonstrated outstanding power performance and is likely to become the preferred transistor for many power applications at frequencies ranging from 10 GHz to 100 GHz. The InGaAs channel of the pseudomorphic HEMT (PHEMT) is beneficial in many respects. This material produces an excellent conduction band profile, forming an InGaAs quantum well that provides good confinement of the electrons, a necessity for high efficiency power devices. The large GaAlAs/InGaAs conduction band discontinuity allows high two-dimensional electron gas densities (N_s) in the InGaAs channel (of width L_z), and hence high current handling capability for power HEMTs.

Many important properties of $Ga_{1-y}Al_yAs/In_xGa_{1-x}As$/GaAs PHEMTs, either uniformly- or delta-doped (single- or double-side) can be determined by PR/CER or a combination of photoluminescence (PL) [5, 17–27]. It is possible to evaluate the two-dimensional electron gas (2DEG) density, width, and In composition of the channel in addition to the Al composition y of the $Ga_{1-y}Al_yAs$, Fermi level pinning at the substrate/buffer interface, and multiple quantum well GaAs/GaAlAs regions (if present).

Huang et al. [23] have reported a room temperature CER, PL, and X-ray investigation of a double-side delta-doped GaAlAs/InGaAs/GaAs PHEMT. The nominal properties of the sample were as follows: on top of the semi-insulating GaAs (001) substrate was grown 5000 Å of undoped (UD) GaAs followed by ten periods of a GaAs (13 Å)/$Ga_{0.8}Al_{0.2}As$ (200 Å) superlattice buffer layer, Si-delta doping layer #1 (1×10^{12} cm^{-2}), 50 Å of UD $Ga_{0.8}Al_{0.2}As$, the UD $In_{0.2}Ga_{0.8}As$ channel (L_c = 130 Å), 45 Å of UD $Ga_{0.8}Al_{0.2}As$, Si-delta doping layer #2 (1×10^{12} cm^{-2}), 350 Å of n-$Ga_{0.8}Al_{0.2}As$ (2.4×10^{17} cm^{-3}), 120 Å of GaAs (2.4×10^{17} cm^{-3}) and 350 Å of n-GaAs (2.4×10^{18} cm^{-3}).

The solid line in Fig. 6 is the room temperature PL signal which exhibits three features, denoted A, B and C. The dashed line is the numerical derivative (with respect to photon energy) of the PL data from

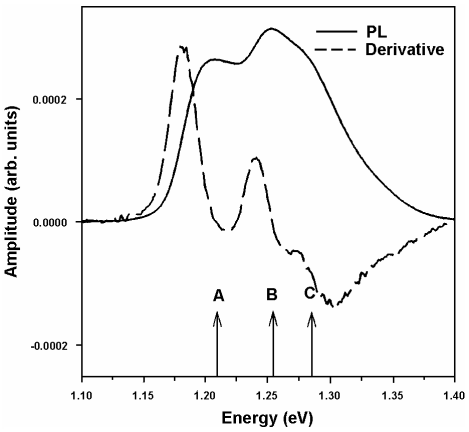

Fig. 6 Solid line is the room-temperature PL spectrum of a double-side delta-doped GaAlAs/InGaAs/GaAs PHEMT structure. The dash line is the numerical derivative of the PL data yielding the energies denoted by arrows.

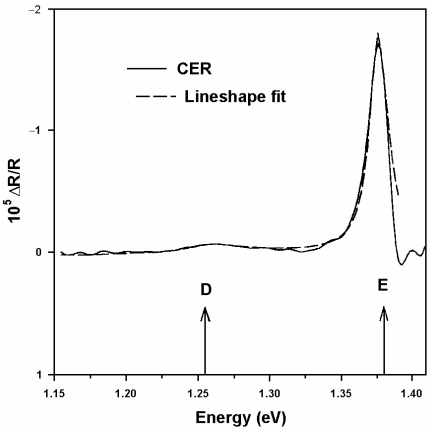

Fig. 7 Room-temperature CER spectrum (solid line) in the region of the InGaAs channel region of a double-side delta-doped GaAlAs/InGaAs/GaAs PHEMT structure. The dashed line is a line-shape fit yielding the energies indicated by the arrows and $E_F - E_{2C}$.

which the authors accurately obtained the energies of the three features (as denoted by arrows) from the zero crossing (A and B) and inflection point (C). These values are listed in Table 1. The lowest lying feature (A) is associated with the fundamental "symmetry-allowed" 1C–1H transition, where the notation mC–nH denotes a transition between the m-th electron and n-th heavy-hole valence subbands of the InGaAs channel. The B and C features have been identified as 2C–1H and 1C–3H, respectively.

The dashed line in Fig. 7 is a least-squares fit to a lineshape which consists of the first-derivative (with respect to photon energy) of a broadened step-like two-dimensional joint density of states (screened exciton) multiplied by a Fermi level filling function [1, 2, 17]. This lineshape fit yields the energies of the D (1.255 eV) and E (1.380 eV) features as well as the position of $E_F - E_{2C}$ (where E_F is the Fermi energy), as listed in Table 1. The CER lineshape fit places E_F about 1 meV above the energy of 2C. Thus from the values of 2C–1C (deduced from A and B/D) and $E_F - E_{2C}$ it is possible to evaluate the 2DEG density, $N_s = (1.80 \pm 0.10) \times 10^{12}$ cm^{-2}. In the CER spectrum from the InGaAs channel, transitions to the 1C state are not seen since it is completely filled while resonances involving the 2C state are weak since

Table 1 Comparison of experiment and calculation of the transition energies of a double-side delta-doped GaAlAs/InGaAs PHEMT structure.

feature	transition	energy (eV)		relative intensities (arbitrary units)[c]
		experiment	calculation	
A[a]	1C–1H	1.210 ± 0.002	1.205[c]	0.06
B[a]/D[b]	2C–1H	1.255 ± 0.002	1.257[c]	1.00
C[a]	1C–3H	1.286 ± 0.002	1.292[c]	0.50
E[b]	3C–2H	1.380 ± 0.002	1.384[c]	0.24
	$E_F - E_{2C}$[b]	0.001 ± 0.002	–0.003[c]	
G[b]	"1C–1H"	1.659 ± 0.002	1.667[d]	
H[b]	"1C–1L"	1.681 ± 0.002	1.686[d]	
I[b]	$Ga_{0.78}Al_{0.22}As$ (Bulk)	1.741 ± 0.003		

[a] From PL spectrum.
[b] From CER spectrum.
[c] Comprehensive, self-consistent Poisson-Schrödinger calculation.
[d] Envelope function calculation including exciton binding energy of 10 meV.

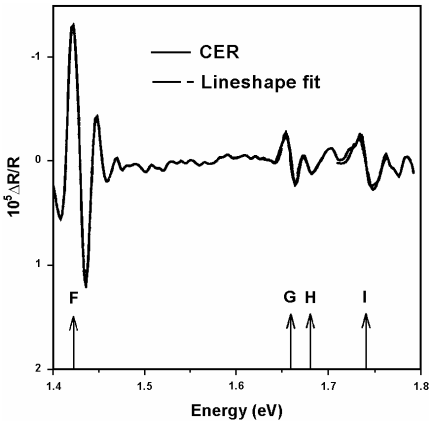

Fig. 8 Room-temperature CER spectrum (solid line) from the rest of the double-side delta-doped GaAlAs/InGaAs/GaAs PHEMT sample. The dashed lines are line-shape fits yielding the energies indicated by the arrows.

it is partially filled. The strong amplitude of the *E* feature indicates that it involves an empty conduction state, i.e., 3C.

Shown by the solid line in Fig. 8 is the CER data originating from the rest of the sample. The feature labeled F corresponds to the band gap of GaAs and exhibits FKOs. The structures G and H originate from the GaAs/GaAlAs SL buffer layer while I is from the bulk GaAlAs portion of the sample.

The X-ray analysis of the InGaAs channel revealed that the In composition is $20 \pm 0.3\%$ and $L_c = 140 \pm 5$ Å. To aid in the identification of the origins of the various PL/CER features the authors performed a self-consistent Poisson-Schrödinger calculation including Fermi level pinning at the GaAs free surface and buffer. Good agreement with the experimental energies was obtained by assuming (a) delta sheet dopings of 3.1×10^{12} cm^{-2} and 1×10^{12} cm^{-2} for layers #2 and #1, respectively, (b) an In composition of 20%, and (c) $L_c = 145$ Å. These deduced structural parameters are in good agreement with the X-ray results. In addition this calculation places the Fermi energy 3 meV below 2C. These results are displayed in Table 1. The above value for the sheet doping density of layer #2 is lower than the intended number of 5×10^{12} cm^{-2} in the calculation causes all the transitions to redshift by about 100 meV, in disagreement with the experiment.

3.3 Quantum well lasers including vertical cavity surface emitting lasers structures

Quantum well laser structures employ complex sequences of thin layers of single crystal materials, where a few light-emitting QWs are embedded in waveguide regions and enclosed by p- and n-doped contact layers. Analysis of the active region, buried under much thicker layers, is difficult after the sequence of layers is completed. Commonly PL and EL are used to analyze the positions of energy levels and quality of the wells. During their lifetime, however, excited electrons and holes may migrate to defects or to wider portions of the wells and the emission spectrum may not be representative of the sample. More direct access to the density of states by absorption is difficult since the absorption of light by a few wells buried under thick conducting layers may be too weak to be resolved. Frequently, therefore, photoconductivity (PC) measurements are used as substitutes.

PR and CER have been used for the nondestructive, room temperature investigation of wafer scale single quantum well (SQW), multiple quantum well (MQW) and quantum dot (QD) laser structures. These include 0.98 μm InGaAs/GaAs/GaAlAs GRINSCH [28], 1.3 μm InGaAsP/InP [30, 62], 0.98 μm InGaAs/GaAs/GaInP [62], 0.65 μm InGaP/AlInP/AlGaInP [63] edge emitting structures, InGaAs/GaAs/GaAlAs [29, 32–36, 39] and GaAs/GaAlAs VCSELs [32], and InAs/GaAs self-assembled QD lasers [64]. Aigouy et al. have performed a micro-ER/PR characterization of the bias dependence of the quantum confined Stark effect in a fabricated 0.98 μm InGaAs/GaAs/GaInP laser with a spatial resolution of ≈10 μm [31]. The method of SPS and wavelength modulated DSPS have been used to investi-

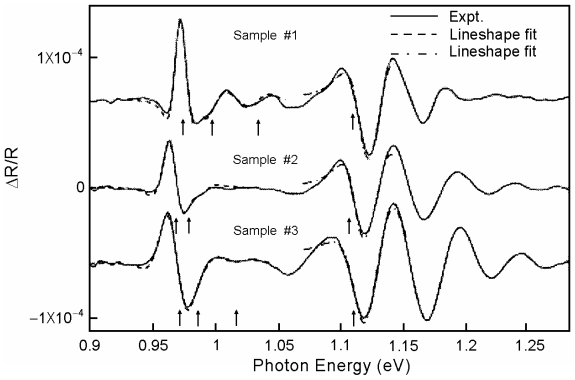

Fig. 9 Solid lines are the CER spectra from three InGaAsP/InP MQW lasers with different amounts of p-dopant (Zn) interdiffusion. The dashed lines are fits to the first-derivative of a Gaussian lineshape yielding the energies of the MQW intersubband energies denoted by arrows. The dot-dashed lines are fits to a lineshape which contains a Lorentzian broadened electro-optic function yielding the InGaAsP band gap energies denoted by the arrows. The curves for samples #1 and #3 have been displaced for clarity.

gate 0.98 μm InGaAs/GaAs/GaAlAs GRINSCH edge emitting structures [46], InGaAs/GaAs/GaAlAs VCSELs [39], 850 nm GaAlAs/GaAs VCSELs [47–49] and 1.3 μm InGaAlAs/InP VCSELs [50, 51].

3.3.1 p-Dopant interdiffusion in 1.3 μm InGaAsP/InP structures

Jaeger et al. have reported a CER and piezoreflectance (PzR) investigation of three $In_{1-x}Ga_xAs_yP_{1-y}$/InP p–*i*–n MQW laser structures with different p-doping profiles [30]. From the observed FKOs originating in the total insulating region [*i*-InGaAsP separate confinement heterostructure (SCH) plus MQWs] they have determined the built-in electric field in this region of the samples. There is a systematic increase in the measured electric field with interdiffusion of the p-dopant due to the reduction of the effective dimension of the *i*-region. These results are in good agreement with secondary ion mass spectrometry (SIMS) measurements on these samples. In addition the CER/PzR spectra from the MQWs region also exhibit the effect of the interdiffusion. From a comparison of the intersubband transitions observed in CER/PzR with an envelope function calculation, including the effects of strain and electric field, it was possible to gain information about parameters such as the well width and in-plane strain of the MQWs regions. The values of these quantities are in good agreement with high resolution X-ray diffraction measurements.

Table 2 Comparison of the experimental and calculated values of the mC-nHH(LH) transitions from the $In_{1-x}Ga_xAs_yP_{1-y}$/InP MQW region. The calculation includes strain, exciton binding energy (5 meV), and the quantum confined Stark effects (5 meV). Also listed are the experimental values of the in-plane strain and L_w.

sample no.	feature	experiment				calculation				
		CER	PzR	HRXRD						
		energy (eV)	energy (eV)	ε (%)	L_w (Å)	energy (eV)	transition	x/y	ε (%)	L_w (Å)
1	A	0.974 [5.5[a]]	0.975	–0.49	75	0.972	1C–1HH	0.200/0.561	–0.40	75
	B	0.998	1.002			0.998	1C–2HH			
	C		1.013			1.015	1C–1LH			
	D	1.034				1.039	1C–3HH			
2	A	0.969 [7.3[a]]	0.963	–0.55	69	0.962	1C–1HH	0.207/0.584	–0.43	69
	B	0.979	0.981			0.993	1C–2HH			
	C		1.007			1.009	1C–1LH			
3	A	0.971 [9.8[a]]	0.966	–0.50	75	0.967	1C–1HH	0.178/0.551	–0.52	75
	B	0.986				0.994	1C–2HH			
	C		1.016			1.016	1C–1LH			

[a] Gaussian linewidth in meV.

Table 3 Comparison of the experimental and calculated electric fields in the *i*-InGaAsP regions.

sample no.	electric field (kV/cm)	
	experiment	calculation
1	32	26
2	49	45
3	56	57

The solid lines in Fig. 9 are the 300 K experimental CER spectra from samples #1, #2, and #3. The curves for samples #1 and #3 have been displaced for clarity. The features below about 1.1 eV are from the MQWs while above this energy the signal is from the InGaAsP SCH. The dashed lines are least-square fits to the first derivative of a Gaussian profile. The obtained values of the MQWs intersubband energies are denoted by arrows and listed in Table 2. The dot-dashed lines are least-square fits to a line-shape which contains a Lorentzian broadened electro-optic function yielding the InGaAsP band gaps or 1.110 eV (sample #1), 1.107 eV (sample #2), and 1.110 eV (sample #3) as indicated by the arrows.

The CER data from the SCH region in all three samples exhibit FKOs. Electric fields of 32 kV/cm, 49 kV/cm, and 56 kV/cm were obtained for samples #1, #2, and #3, respectively. This increase in the measured electric field originating from the SCH region in going from sample #1 to #3 can be explained in terms of the differences in the Zn-doping profile. The SIMS data yields the width of the *i*-layer, W_i = 495 nm, 290 nm, and 225 nm for samples #1, #2, and #3, respectively. Based on the built-in potential deduced from the InP n- and p-doping levels the corresponding electric fields are 26 kV/cm, 45 kV/cm, and 57 kV/cm, respectively, in good agreement with the experimental values. These results are summarized in Table 3.

3.3.2 Vertical-cavity surface-emitting lasers

Vertical-cavity surface-emitting lasers have a number of advantages in relation to other types of semiconductor lasers including single longitudinal mode operation, low divergence, circularly symmetric beam profile, low threshold current, and ease of integration. The basic structure of a VCSEL is a Fabry–Pérot (FP) cavity consisting of an active region with embedded quantum wells (QWs), sandwiched between two multilayer distributed Bragg reflector (DBR) stacks that form highly reflecting mirrors with a broad reflectance stop band centered on a certain free space photon energy E_{Bragg}. In general, both DBR stacks are heavily p(upper)/n(lower) doped, so that the entire structure forms a p$-i-$n diode. The overall optical thickness of this active region determined the approximate cavity length, which is usually a few integer multiples of half of the intended lasing wavelength. Interaction of the DBRs and cavity produces a sharp FP dip in the reflection spectrum at the photon energy E_{cav}, which is usually positioned at the center of the stop band. The fundamental QW conduction to heavy-hole excitonic transition, which occurs at the energy of E_{QW}, provides the gain. To achieve the desired performance, VCSELs are designed such that E_{QW} coincides with E_{cav} at operation temperature. This means that E_{QW} at room temperature should be chosen somewhat higher than the other two so that local temperature increase during operation may compensate for the offset. In order to reduce production costs and to assure reproducibility, better means of growth and characterization need to be developed. Therefore, a contactless and nondestructive method to rapidly determine E_{QW} and E_{cav} of an epitaxial structure before laser processing is of importance to the manufacturer.

The nondestructive characterization of VCSELs presents a considerable challenge since photoluminescence (PL), a technique that has been most commonly used to characterize edge-emitting lasers, is not very useful for VCSELs because of the high DBR reflectivity. The reflectance (R) of VCSEL is determined by the physical structure of the DBRs and cavity, which yields E_{cav}, but generally provides no information on E_{QW}. Hence the R spectrum is not useful for checking the degree of mismatch between

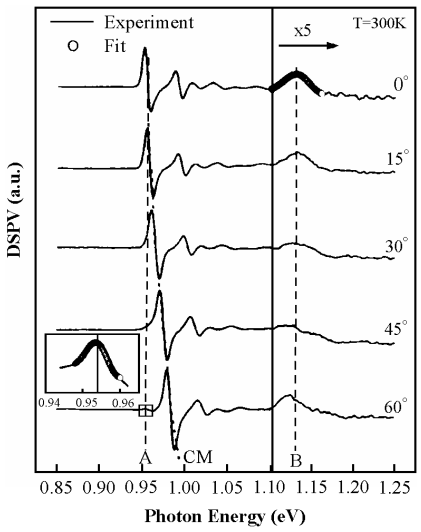

Fig. 10 Room temperature DSPV spectra of a 1.3 μm InGaAlAs/InP VCSEL structure for different angles of incidence θ of the light beam. The spectra are shifted vertically for clarity. With increasing θ the cavity mode and other DBR features shift to higher energy. The dotted line provides a guide to the eye for the angular dependence of the cavity mode. DSPV features denoted by dashed lines do not shift with θ which is due to the QW transition and the interband transition of the InGaAlAs barriers. The inset shows the DSPV spectrum in the range 0.94–0.965 eV for feature A at incident angle $\theta = 60°$. The open circle curves are the first derivative of a Gaussian line shape fit for the 1C–1H excitonic transition and the InGaAlAs interband transition.

the two energies. Therefore, it will be most appropriate to explore other optical characterization techniques that are capable of extracting information on both E_{QW} and E_{cav}. Other useful optical diagnostic techniques such as CER and PR yield, at room temperature, signals making it possible to evaluate E_{QW} [32–39], and in some cases E_{cav} as well as the built-in electric field in the *i*-region from the FKOs [32–38]. Jaeger et al. have reported room temperature angle-dependent photocurrent (PC) spectroscopy that yields E_{QW} and E_{cav} [65]. Huang et al. [39], Liang et al. [47, 48], and Huang et al. [50] have reported SPS characterization of the 980 nm InGaAs/GaAs/GaAlAs, 850 nm GaAs/GaAlAs, and 1.3 μm InGaAlAs/InP VCSELs, respectively. Wang et al. [52] have demonstrated that angle-dependent wavelength-modulated DSPS at room temperature can be employed to evaluate both E_{QW} and E_{cav} accurately as well as the interference pattern from the DBRs. The wavelength-modulated DSPS technique offers may superior feature over the other methods for VCSEL structure characterization and deserved further exploration.

Recently Liang et al. [52] have reported a comprehensive DSPS study of an 1.3 μm InGaAlAs/InP VCSEL structure as a function of incident angles θ. To help in the identification of the observed 1C–1H exciton and cavity mode features they have also performed angle-dependent SPS and R measurements. Figure 10 shows a set of differential surface photovoltage (DSPV) spectra measured under different incident angles θ of the light beam at room temperature. In terms of the dependence on the incident angles θ, the observed features can be grouped into two types. Type-I features correspond to those that shift toward higher energy with increasing θ. These include the cavity mode (CM) (dotted line) and the DBR mirror features. Type-II features (highlighted as letters A and B) show no shift at all with the incident angle. Feature A corresponds to the onset of absorption of fundamental (1C–1H) transition in the InGaAlAs QWs and becomes visible at θ larger than 45° as a small peak located in the lower energy region. The inset of Fig. 10 shows the DSPV spectrum in the range of 0.94–0.965 eV, shown by the open circles is the derivative of a Gaussian lineshape fit, which is appropriate for excitonic transition. The obtained value for the 1C–1H transition (feature A) energy is $E_{QW} = 0.954 \pm 0.001$ eV with the broadening parameter $\Gamma = 0.004 \pm 0.001$ eV. Feature B appears as a broad structure in Fig. 10 and is observed at higher photon energy (denoted by an arrow) at 1.13 eV. The feature corresponds to the direct gap of the InGaAlAs barriers.

Figure 11 summarizes the results of the angle-dependent DSPS, SPS, and R measurements. The open circles and closed triangles are $E_{QW}(\theta)$ determined from DSPS and SPS, respectively. The values for $E_{cav}(\theta)$ as determined from DSPS, SPS, and R are represented as open triangles, closed circles, and open squares, respectively. The angle independent nature of $E_{QW}(\theta)$ is quite clear from DSPS and SPS measurements as illustrated in Fig. 11. The dependence of $E_{cav}(\theta)$ determined from DSPS, SPS, and R spectra

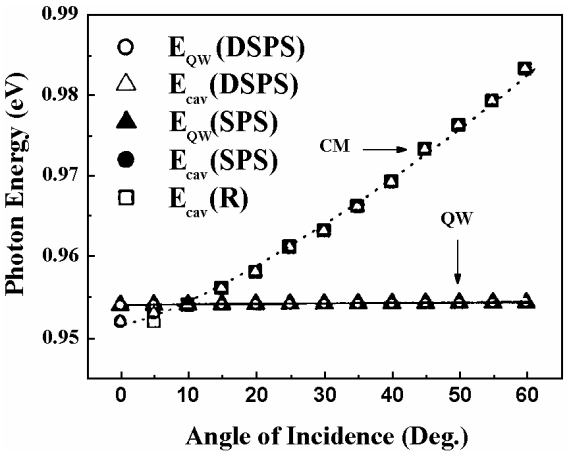

Fig. 11 Angle dependence of the fundamental excitonic quantum well transition and cavity mode for a 1.3 μm InGaAlAs/InP VCSEL structure determined from the SPS, DSPS, and R measurements. The open circles and closed triangles are $E_{QW}(\theta)$ determined from DSPS and SPS, respectively, while the open triangles, closed circles and open squares are $E_{cav}(\theta)$ determined from DSPS, SPS, and R, respectively. The dotted line is a least-squares fit to Eq. (2).

agree well with each other. The angular dependent $\lambda_{cav}(\theta)$ can be fitted with [33, 47]

$$\lambda_{cav}(\theta) = \left(\frac{2d}{m}\right)\left(\frac{1-\sin^2\theta}{n^2}\right)^{1/2} = \lambda(0°)\left(\frac{1-\sin^2\theta}{n^2}\right)^{1/2} . \quad (2)$$

In Eq. (2), m is an integer, $\lambda(0°)$ is the wavelength at normal incidence, d is the effective thickness, and n is the effective refraction index for the cavity. The effective cavity length and effective refraction index are deduced to be 3873 ± 40 Å and 3.365 ± 0.002, respectively. The value of the determined effective cavity length is in reasonable agreement with the intended number.

The DSPS has a number of advantages over other methods for VCSEL characterization such as SPS, R, PR, and PC. The DSPS and SPS are both related to the photovoltaic effect, which is very sensitive to the low light levels that reach the QW region through the top DBR mirrors. The wavelength-modulated DSPS yields a derivative spectrum, which can further improve the accuracy and sensitivity of the SPS dramatically. The DSPV spectrum can be fitted by a line shape function and the energies of various transitions may be evaluated to within a few meV at room temperature. While both the CM and 1C–1H transition are always observed in DSPS, for PR in some cases, only the latter is observed. In DSPS and SPS a rich interference pattern related to the properties of the DBR are observed in contrast to PR. In addition, DSPS has an advantage over PR in that it requires no pumping beam. The techniques of DSPS, SPS and PR are contactless and require no special mounting of the sample and hence are completely nondestructive and can be employed on the entire wafer. This attribute is superior to PC where contact must be made with the sample and hence some degree of damage to the sample is inevitable.

4 Summary

This article has reviewed the use of the contactless methods of PR, CER, and wavelength modulated DSPS for the nondestructive, room temperature characterization of a wide variety of wafer-scale III–V semiconductor device structures. Systems that were discussed include HBTs such as graded emitter GaAlAs/GaAs, GaInP/GaAs as well as GaInP/GaInNAs/GaAs (including the determination of the built-in fields/doping levels in the emitter and collector regions, doping level and minority carrier lifetime in the base, alloy composition, and the degree of ordering in the GaInP), GaAlAs/InGaAs/GaAs PHEMTs (including the determination of the composition, width, and two-dimensional electron gas density in the channel), quantum well edge emitting lasers [InGaAsP/InP (including the detection of p-dopant interdiffusion)]. The DSPS results on an 1.3 μm InGaAlAs/InP VCSEL structure is particularly interesting since with one relatively simple measurement it is possible to determine the fundamental conduction to heavy-hole excitonic transition in the QW, the cavity mode, and information about the DBRs. These methods are already being used by more than a dozen industries world-wide for the production-line qualification

of these device structures, including TRW, Agilent, Rockwell International, Lucent Technologies, HRL Laboratories, Kopin, Epitronics, RF Micro Devices, Emcore, Alpha Industries, Nortel (Canada), Picogiga (France), IQE (UK), United Epitaxial Laboratory (Taiwan), Hitachi Cable (Japan), and Sumitomo Chemical (Japan).

Acknowledgements The author YSH acknowledges the support of National Science Council of Taiwan. FHP acknowledges the support of the New York State Science and Technology Foundation through its Centers for Advanced Technology program.

References

[1] F. H. Pollak and H. Shen, Mater. Sci. Eng. R **10**, 275 (1993).
[2] F. H. Pollak, Modulation Spectroscopy of Semiconductors and Semiconductor Microstructures, edited by M. Balkanski, Handbook on Semiconductors Vol. 2 (Elsevier, Amsterdam, 1994), p. 527.
[3] O. J. Glembocki, and B. V. Shanabrook, Semiconductors and Semimetals Vol. 36, edited by D. G. Seiler and C. L. Littler (Academic Press, New York, 1992), p. 222.
[4] F. H. Pollak, Encyclopedia of Materials Characterization: Surfaces, Interfaces and Thin Films, edited by C. Evans, R. Brundle, and S. Wilson, (Butterworth-Heinemann, Boston, 1992), p. 235.
[5] J. Misiewicz, P. Sitarek, G. Sęk, and R. Kudrawiec, Mater. Sci. **21**, 263 (2003).
[6] X. Yin, F. H. Pollak, L. Pawlowicz, T. O'Neill, and M. Hafizi, Appl. Phys. Lett. **56**, 1278 (1990).
[7] N. Bottka, D. K. Gaskill, P. D. Wright, R. W. Kaliski, and D. A. Williams, J. Cryst. Growth **107**, 893 (1991).
[8] W. D. Sun and F. H. Pollak, J. Appl. Phys. **83**, 4447 (1998).
[9] Y. S. Huang, W. D. Sun, L. Malikova, F. H. Pollak, T. S. Low, and J. S. C. Chang, Appl. Phys. Lett. **73**, 1215 (1998).
[10] A. C. Han, M. Wojtowicz, T. R. Block, X. Zhang, T. P. Chin, A. Cavus, A. Oki, and D. C. Streit, J. Appl. Phys. **86**, 6160 (1999).
[11] Y. S. Huang, W. D. Sun, F. H. Pollak, J. L. Freeouf, I. D. Calder, and R. E. Mallard, Appl. Phys. Lett. **73**, 214 (1998).
[12] C. J. Lin, Y. S. Huang, N. Y. Li, P. W. Li, and K. K. Tiong, J. Appl. Phys. **90**, 4565 (2001).
[13] Y. S. Huang, C. J. Lin, C. H. Wang, N. Y. Li, C. C. Fan, and P. W. Li, IEE Proc., Optoelectron. **150**, 99 (2003).
[14] D. Yan, F. H. Pollak, V. T. Boccio, C. L. Lin, P. D. Kirchner, J. M. Woodall, R. C. Gee, and P. M. Asbeck, Appl. Phys. Lett. **61**, 2066 (1992).
[15] K. T. Hsu, Y. H. Chen, K. L. Chen, H. P. Chen, H. H. Lin, and G. J. Jan, Appl. Phys. Lett. **64**, 1974 (1994).
[16] K. L. Chen, H. H. Lin, G. J. Jan, Y. H. Chen, and P. K. Tseng, Appl. Phys. Lett. **66**, 2697 (1995).
[17] Y. Yin, H. Qiang, F. H. Pollak, D. C. Streit, and M. Wojtowicz, Appl. Phys. Lett. **61**, 1579 (1992).
[18] G. Gumbs, D. Huang, Y. Yin, H. Qiang, D. Yan, F. H. Pollak, and T. F. Noble, Phys. Rev. B **48**, 18328 (1993).
[19] Y. Yin, H. Qiang, D. Yan, F. H. Pollak, and T. F. Noble, Semicond. Sci. Technol. **8**, 1599 (1993).
[20] A. Dimoulas, K. Zekentes, M. Androulidaki, N. Kornelios, C. Michelakis, and Z. Hatzopoulos, Appl. Phys. Lett. **63**, 1417 (1993).
[21] A. Dimoulas, J. Davidow, K. P. Giapis, A. Georgakilas, G. Halkias, and N. Kornelios, J. Appl. Phys. **80**, 3484 (1996).
[22] A. C. Han, M. Wojtowicz, D. Pascua, T. R. Block, and D. C. Streit, J. Appl. Phys. **82**, 2607 (1997).
[23] Y. S. Huang, W. D. Sun, L. Malikova, F. H. Pollak, I. Ferguson, H. Hou, Z. C. Feng, T. Ryan, and E. B. Fantner, Appl. Phys. Lett. **74**, 1851 (1999).
[24] D. Y. Lin, Y. S. Huang, K. K. Tiong, F. H. Pollak, and K. R. Evans, Semicond. Sci. Technol. **14**, 103 (1999).
[25] D. Y. Lin, S. H. Liang, Y. S. Huang, K. K. Tiong, F. H. Pollak, and K. R. Evans, J. Appl. Phys. **85**, 8235 (1999).
[26] T. H. Chen, Y. S. Huang, D. Y. Lin, F. H. Pollak, M. S. Goorsky, D. C. Streit, and M. Wojtowicz, J. Appl. Phys. **88**, 883 (2000).
[27] D. Y. Lin, Y. S. Huang, T. S. Shou, K. K. Tiong, and F. H. Pollak, J. Appl. Phys. **90**, 6421 (2001).
[28] W. Krystek, M. Leibovitch, W. D. Sun, F. H. Pollak, G. Gumbs, G. T. Burnham, and X. Wang, J. Appl. Phys. **84**, 2229 (1998).
[29] S. Moneger, H. Qiang, F. H. Pollak, D. L. Mathine, R. Droopad, and G. N. Maracas, Solid-State Electron. **39**, 871 (1996).

[30] A. Jaeger, W. D. Sun, F. H. Pollak, C. L. Reynolds, Jr., and M. Geva, J. Appl. Phys. **86**, 2020 (1999).
[31] L. Aigouy, F. H. Pollak, and G. Gumbs, Appl. Phys. Lett. **70**, 2562 (1997).
[32] P. D. Berger, C. Bru, T. Benyattou, G. Guillot, A. Chenevas-Paule, L. Couturier, and P. Grosse, Appl. Phys. Lett. **68**, 4 (1995).
[33] P. J. Klar, G. Rowland, T. E. Sale, T. J. C. Hosea, and R. Grey, phys. stat. sol. (a) **170**, 145 (1998).
[34] P. M. A. Vincente, P. J. S. Thomas, D. Lancefield, T. E. Sale, T. J. C. Hosea, and R. Grey, phys. stat. sol. (b) **211**, 255 (1999).
[35] P. J. Klar, G. Rowland, P. J. S. Thomas, A. Onischenko, T. E. Sale, T. J. C. Hosea, and R. Grey, Phys. Rev. B **59**, 2894 (1999).
[36] P. J. Klar, G. Rowland, P. J. S. Thomas, A. Onischenko, T. E. Sale, T. J. C. Hosea, and R. Grey, Phys. Rev. B **59**, 2902 (1999).
[37] T. E. Sale, T. J. C. Hosea, and P. J. S. Thomas, IEEE Photonics Technol. Lett. **12**, 1328 (2000).
[38] S. Ghosh, T. J. C. Hosea, and S. B. Constant, Appl. Phys. Lett. **78**, 3050 (2001).
[39] Y. S. Huang, L. Malikova, F. H. Pollak, H. Shen, J. Pamulapati, and P. Newman, Appl. Phys. Lett. **77**, 37 (2000).
[40] B. Adamowicz and J. Szuber, Surf. Sci. **247**, 94 (1991).
[41] L. Kronik and Y. Shapira, Surf. Sci. Rep. **37**, 1 (1999).
[42] N. Ashkenasy, M. Leibovitch, Y. Rosenwaks, and Y. Shapira, Mater. Sci. Eng. B **74**, 1125 (2000).
[43] L. Kronik and Y. Shapira, Surf. Interface Anal. **31**, 954 (2001).
[44] B. Mishori, M. Leibovitch, Y. Shapira, F. H. Pollak, D. C. Streit, and M. Wojtowicz, Appl. Phys. Lett. **73**, 650 (1998).
[45] Y. T. Cheng, Y. S. Huang, D. Y. Lin, K. K. Tiong, F. H. Pollak, and K. R. Evans, Appl. Phys. Lett. **79**, 949 (2001).
[46] N. Ashkenasy, M. Leibovitch, Y. Shapira, F. H. Pollak, G. T. Burnham, and X. Wang, J. Appl. Phys. **83**, 1146 (1998).
[47] J. S. Liang, Y. S. Huang, C. W. Tien, Y. M. Chang, C. W. Chen, N. Y. Li, P. W. Li, and F. H. Pollak, Appl. Phys. Lett. **79**, 3227 (2001).
[48] J. S. Liang, S. D. Wang, Y. S. Huang, C. W. Tien, Y. M. Chang, C. W. Chen, N. Y. Li, D. Y. Lin, and F. H. Pollak, Appl. Phys. Lett. **80**, 752 (2002).
[49] J. S. Liang, S. D. Wang, Y. S. Huang, C. W. Tien, Y. M. Chang, C. W. Chen, N. Y. Li, K. K. Tiong, and F. H. Pollak, J. Phys.: Condens. Matter **15**, 55 (2003).
[50] Y. S. Huang, L. Malikova, F. H. Pollak, J. P. Debray, R. Hoffman, A. Amtout, and R. A. Stall, J. Appl. Phys. **91**, 6203 (2002).
[51] S. D. Wang, J. S. Liang, Y. S. Huang, C. W. Tien, Y. M. Chang, C. W. Chen, N. Y. Li, K. K. Tiong, and F. H. Pollak, J. Appl. Phys. **92**, 2350 (2002).
[52] J. S. Liang, S. D. Wang, Y. S. Huang, L. Malikova, F. H. Pollak, J. P. Debray, R. Hoffman, A. Amtout, and R. A. Stall, J. Appl. Phys. **93**, 1874 (2003).
[53] F. H. Pollak, Modulation Spectroscopy of the Group III-Nitrides, in: Group III Nitride Semiconductor Compounds, edited by B. Gil (Clarendon, Oxford, 1998), p. 158.
[54] W. Krystek, F. H. Pollak, Z. C. Feng, M. Schurman, and R. A. Stall, Appl. Phys. Lett. **72**, 1353 (1998).
[55] D. Yan, H. Qiang, and F. H. Pollak, Rev. Sci. Instrum. **65**, 1988 (1994).
[56] W. M. Theis, G. D. Sanders, C. E. Leak, K. K. Bajaj, and H. Morkoç, Phys. Rev. B **37**, 3042 (1988).
[57] O. J. Glembocki and B. V. Shanabrook, Proc. Soc. Photo-Opt. Instrum. Eng. (SPIE, Bellingham) **794**, 74 (1987).
[58] H. Shen and M. Dutta, Appl. Phys. Lett. **57**, 587 (1990).
[59] M. Sydor and A. Badakhshan, J. Appl. Phys. **70**, 2322 (1991).
[60] H. C. Kuo, J. M. Kuo, Y. C. Wang, C. H. Lin, and G. E. Stillman, J. Electron. Mater. **26**, 944 (1997).
[61] A. Lindell, M. Pessa, A. Salokatve, F. Bernardini, R. M. Nieminen, and M. Paalanen, J. Appl. Phys. **82**, 3374 (1997).
[62] F. H. Pollak, W. Krystek, S. Moneger, H. Qiang, and D. Yan, Proc. Soc. Photo-Opt. Instrum. Eng. (SPIE, Bellingham) **2397**, 92 (1995).
[63] P. M. Amirtharaj, D. Chandler-Horowitz, and D. Bour, Mater. Res. Soc. Symp. Proc. **406**, 229 (1995).
[64] L. Aigouy, T. Holden, F. H. Pollak, N. N. Ledentsov, V. M. Ustinov, P. S. Kop'ev, and D. Bimberg, Appl. Phys. Lett. **70**, 3329 (1997).
[65] A. Jaeger, P. M. Petroff, and T. D. Lowes, Appl. Phys. Lett. **78**, 3012 (2001).

Photoluminescence and surface photovoltage spectroscopy characterization of $Zn_{1-x-y}Be_xMg_ySe$ mixed crystals

D. O. Dumcenco,[1] H. P. Hsu,[1] Y. S. Huang,[1,a)] F. Firszt,[2] S. Łęgowski,[2] H. Męczyńska,[2] K. Strzałkowski,[2] and K. K. Tiong[3]
[1]*Department of Electronic Engineering, National Taiwan University of Science and Technology, Taipei 106, Taiwan*
[2]*Institute of Physics, N. Copernicus University, Grudziądzka 5/7, 87-100 Toruń, Poland*
[3]*Department of Electrical Engineering, National Taiwan Ocean University, Keelung 202, Taiwan*

(Received 10 February 2008; accepted 28 February 2008; published online 8 May 2008)

This paper presents an optical characterization of three Bridgman-grown $Zn_{1-x-y}Be_xMg_ySe$ mixed crystals in the near-band-edge interband transitions using temperature-dependent photoluminescence (PL) in the temperature range of 10–300 K and surface photovoltage spectroscopy (SPS) at room temperature. PL spectra at low temperatures of the investigated samples consist of an excitonic line, an edge emission due to radiative recombination of shallow donor-acceptor pairs, and a broad band related to recombination through deep level defects. The anomalous S-shape temperature dependence of the exciton emission peak for $Zn_{1-x-y}Be_xMg_ySe$ crystals with high Mg content ($y=0.26$) can be explained as due to localization of excited carriers caused by statistical fluctuations of local composition. The peak positions of the excitonic emission lines in PL spectra correspond quite well to the energies of the fundamental transitions determined from SPS measurements. The parameters that describe the temperature dependence of the transition energy and broadening parameter of the band-edge excitonic emission are evaluated and discussed.
 [DOI: 10.1063/1.2913333]

I. INTRODUCTION

Be-chalcogenide semiconductor alloys have recently been proposed for improving the performance of ZnSe-based blue-green lasers.[1,2] According to theoretical calculation,[3] it is known that due to the large amount of covalent bonding and high cohesive energy, the beryllium-based bonding can be used to enhance the crystal elastic rigidity in II–VI alloys. It is expected that the incorporation of beryllium will lead to bond strengthening within the II–VI lattice,[4] and will also increase the energy of stacking-fault formation, thus, reducing defect propagation that has been seriously limiting the lifetimes of ZnSe-based devices. Among the Be-based II–VI compound semiconductors, $Zn_{1-x-y}Be_xMg_ySe$ solid solutions are of particular interest for their potential application in photodetectors operating in the blue-violet and ultraviolet spectral range,[5,6] in constructing blue laser,[7] and in long lived white light emitting diodes.[8–10] Up to this date, in spite of the potential applications, very little work has been done on the basic optical and luminescence properties of this quaternary compound.

In this paper, we report a detailed study of near-band-edge transitions in three $Zn_{1-x-y}Be_xMg_ySe$ mixed crystals grown by the modified high pressure Bridgman method with different content of Be and Mg, using temperature-dependent photoluminescence (PL) and room temperature surface photovoltage spectroscopy (SPS). The PL spectra at low temperature consist of a band-edge exciton line and defect related emission bands. The peak positions of the excitonic emission lines in PL spectra correspond quite well to the energies of the fundamental transitions determined from SPS measurements. The parameters that describe the temperature dependence of the transition energy and broadening parameter of the fundamental band-edge exciton are evaluated and discussed.

II. EXPERIMENTS

The $Zn_{1-x-y}Be_xMg_ySe$ mixed crystals were grown from the melt by the high-pressure Bridgman method.[11] The ZnSe (6 N Koch–Light), Mg, and Be (purity of 99.8%) powders were mixed in stoichiometric proportion and put into a graphite crucible. The crucible was kept at the temperature 1830 K for 3 h and then moved out from the heating zone with a speed of 2.4 mm/h. An argon overpressure of 12 MPa was maintained during the growth process. The obtained crystals were cut into plates of about 1 mm thickness. The structures of the measured samples were determined with an x-ray method, which showed that the samples are uniform in composition. The $Zn_{0.88}Be_{0.06}Mg_{0.06}$ exhibited a single sphalerite (zinc-blende (ZB)) phase. The $Zn_{0.88}Be_{0.14}Mg_{0.06}$ is also of a single sphalerite phase with a trace of a wurtzite one. In the $Zn_{0.88}Be_{0.06}Mg_{0.26}$, the wurtzite phase was found as the main phase with admixture of 4*H* and 8*H* polytypes.

To remove mechanical defects on the surface, the samples were mechanically polished using successively finer abrasives with the final polishing process using 0.05 μm aluminum-oxide (Al_2O_3) powder. For optical measurements, samples were additionally etched in a mixture of $K_2Cr_2O_7:H_2SO_4:H_2O$ with a proportion of 3:2:1 followed by a treatment in CS_2 and 50% NaOH solution.[12]

a)Author to whom correspondence should be addressed. Electronic mail: ysh@mail.ntust.edu.tw.

PL spectra were excited using the 325 nm line (~50 mW) of a He–Cd laser. The luminescence signals were analyzed by using a Jobin–Yvon "TRIAX 550" spectrometer equipped with a "SIMPHONY" charge-coupled device camera. An RMC model 22 close-cycle cryogenic refrigerator equipped with a digital thermometer controller was used to control the measurement temperature between 10 and 300 K with a temperature stability of 0.5 K or better.

In the SPS measurement, the contact potential difference between the sample and a reference grid electrode was measured in a capacitive manner as a function of the photon energy of the probe beam by holding the grid fixed and chopping the probe beam at 200 Hz.[13] It is known that, under low optical excitation, the surface photovoltage (SPV) is proportional to the absorption coefficient.[14] Therefore, by monitoring the potential change when monochromatic light impinges on surface of the sample, it is possible to obtain relevant information of the joint density of states. A 150 W xenon arc lamp filtered by a Photon Technology Inc. 0.25 m monochromator provided the monochromatic light. The incident light intensity was maintained at a constant level of $\sim 10^{-5}$ W/cm^2. A beam splitter was placed in the path of the incident light. The intensity of this radiation was monitored by a power meter and was kept constant by a stepping motor connected to a variable neutral-density filter placed in the path of the incident beam. The induced SPV on the metal grid was measured with a copper bottom as the ground electrode, using a buffer circuit and a lock-in amplifier.

III. RESULTS AND DISCUSSION

Figure 1 presents PL spectra measured at 10 K of three $Zn_{1-x-y}Be_xMg_ySe$ mixed crystal samples with different content of Be and Mg: $Zn_{0.88}Be_{0.06}Mg_{0.06}Se$ [Fig. 1(a)], $Zn_{0.80}Be_{0.14}Mg_{0.06}Se$ [Fig. 1(b)], and $Zn_{0.68}Be_{0.06}Mg_{0.26}Se$ [Fig. 1(c)]. Like some other II–VI compounds,[15–17] at low temperature, the PL spectra of $Zn_{1-x-y}Be_xMg_ySe$ mixed crystals consist of a sharp peak followed by a broad edge-emission feature at the energy about 110 meV lower than the first peak and a broad deep level (DL) bands. As shown in Fig. 1, the first peak denoted as exciton line *X* is located at 2.916 eV for $Zn_{0.88}Be_{0.06}Mg_{0.06}Se$ [Fig. 1(a)]. This feature exhibits blueshifted character with increasing content of either Be or Mg and positioned at 3.086 eV for $Zn_{0.80}Be_{0.14}Mg_{0.06}Se$ [Fig. 1(b)] and 3.126 eV for $Zn_{0.68}Be_{0.06}Mg_{0.26}Se$ [Fig. 1(c)], respectively. The line broadening for the samples with larger Mg/Zn or Be/Zn ratio can be attributed in part to the alloy scattering effects and also to the poorer crystalline quality of the samples with higher content of Mg or Be. The edge-emission band exhibits shift toward higher energies with increasing excitation intensity, so it is due to radiative recombination of shallow donor-acceptor pairs (DAPs).[18] The DAP feature in PL spectra shows a blueshift with an increase in Mg and Be content and the intensity of this band rapidly diminishes for higher content of Mg (Fig. 1). The physical mechanism of radiative recombination responsible for the green broad band is not known but, taking into account the positron annihilation experiment and luminescence data for $Zn_{1-x}Mg_xSe$ and

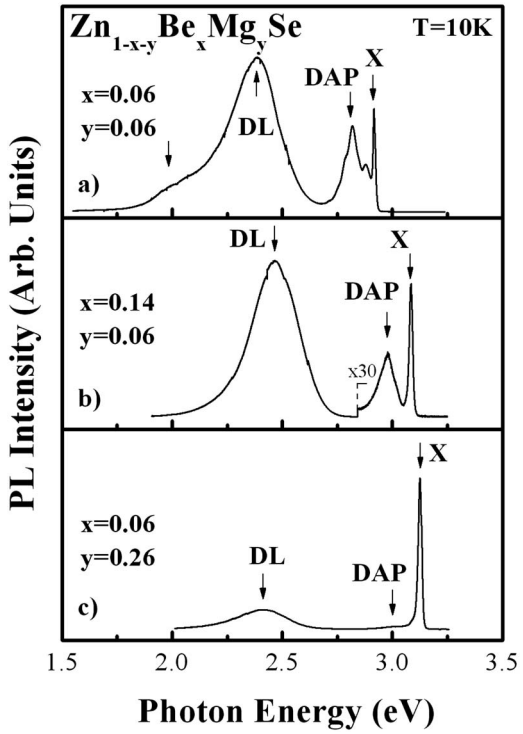

FIG. 1. The PL spectra of $Zn_{1-x-y}Be_xMg_ySe$ with different Be(x) and Mg(y) content: (a) $x=0.06$ and $y=0.06$, (b) $x=0.14$ and $y=0.06$, and (c) $x=0.06$ and $y=0.26$, measured at 10 K. The band-edge excitonic line, DAP emission and DL emission bands are indicated by arrows.

$Zn_{1-x}Be_xSe$,[19,20] one can conclude that this broad band can be attributed to cation vacancy or some kind of defect containing a cation vacancy. The relative intensity of this band decreases with increasing Mg or Be content and noticeably decreases after annealing in zinc vapor at a temperature of 1230 K for 2 days.[19,20]

Figures 2–4 show the temperature evolution of the near-band-edge PL spectra for $Zn_{0.88}Be_{0.06}Mg_{0.06}Se$, $Zn_{0.80}Be_{0.14}Mg_{0.06}Se$, and $Zn_{0.68}Be_{0.06}Mg_{0.26}Se$ crystals, respectively. The low temperature spectrum of $Zn_{0.88}Be_{0.06}Mg_{0.06}Se$ sample (Fig. 2) consists of a free exciton line, as was confirmed by measurements of electromodulation reflectance spectra, and the so-called edge emission at 2.82 eV with clearly observed LO-phonon replicas ($\hbar\omega_{LO}=33$ meV). The rather weak but well resolved peak at 2.88 eV is thermally quenched at a temperature higher than about 60 K. This feature labeled as BX is assigned to the radiative recombination of exciton bound to some deep defect center. With increasing Be or Mg content (Figs. 3 and 4) at low temperature, the intensity of the edge-emission line positioned at 2.98 and 3.02 eV, respectively, becomes smaller in comparison with that in $Zn_{0.88}Be_{0.06}Mg_{0.06}Se$. The BX feature related to deep defect center diminishes with increasing Be and Mg content and only the trace of this line is detectable for $Zn_{0.80}Be_{0.14}Mg_{0.06}Se$. As shown in Figs. 2–4, the excitonic peak monotonically shifts toward lower energy and broadens with increasing temperature in the range from 15 to 300 K. The shallow DAP feature is completely thermally quenched at temperatures higher than 120 K.

A proper surface treatment of the sample must be performed to eliminate the damaged layer formed on the surface

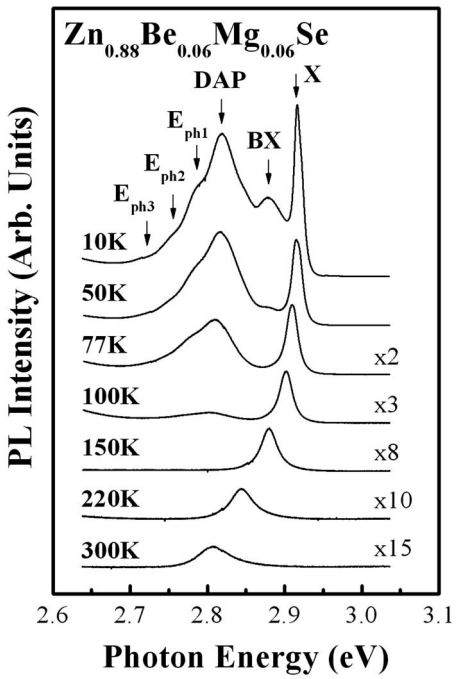

FIG. 2. The PL spectra of $Zn_{0.88}Be_{0.06}Mg_{0.06}Se$ mixed crystal at several temperatures between 10 and 300 K. The band-edge excitonic line, free to band radiative recombination and DAP emission with clearly seen LO-phonon replicas are indicated by arrows.

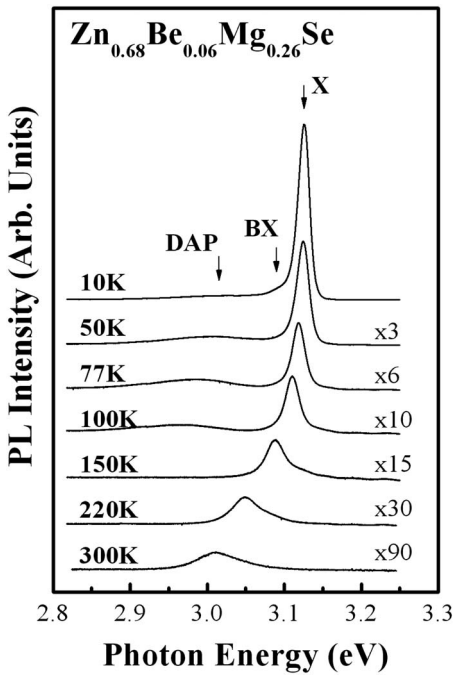

FIG. 4. The PL spectra of $Zn_{0.68}Be_{0.06}Mg_{0.26}Se$ crystal at several temperatures between 10 and 300 K. The band-edge excitonic line, free to band radiative recombination and DAP emission are indicated by arrows.

caused by mechanical polishing. The SPS technique can be utilized to check the condition of the surface layer.[21] Figs. 5(a)–5(c) show the SPV, the first derivative of the SPV (DSPV), and PL spectra near the band edge at 300 K for $Zn_{0.88}Be_{0.06}Mg_{0.06}Se$, $Zn_{0.80}Be_{0.14}Mg_{0.06}Se$, and $Zn_{0.68}Be_{0.06}Mg_{0.26}Se$ mixed crystals, respectively. As shown in Fig. 5, the typical SPV spectrum (dashed curves) has a steplike shape, characteristic for excitonic transitions, in the spectral region around the fundamental transition. In order to determine the values of the transition energies, we have numerically calculated the first derivative of the SPV signal with respect to photon energy $(\Delta V_{SPS}/\Delta E)$ and then divided this quantity by the value of the photovoltage itself V_{SPS}. The ratio $(\Delta V_{SPS}/\Delta E)/V_{SPS}$ is proportional to $(\Delta\alpha/\Delta E)/\alpha$,[14]

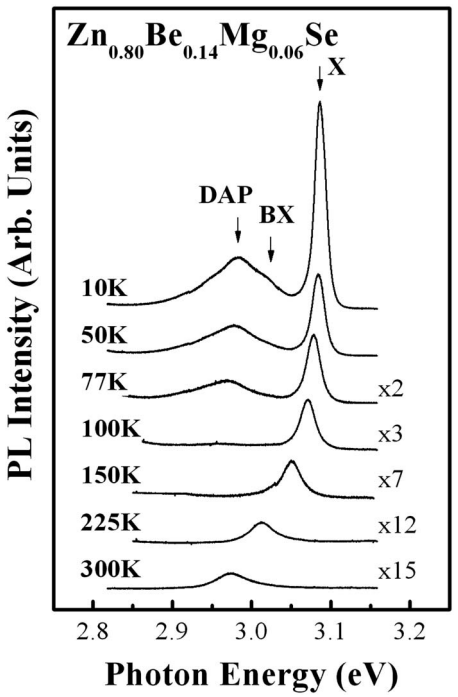

FIG. 3. The PL spectra of $Zn_{0.80}Be_{0.14}Mg_{0.06}Se$ crystal at several temperatures between 10 and 300 K. The band-edge excitonic line, free to band radiative recombination and DAP emission are indicated by arrows.

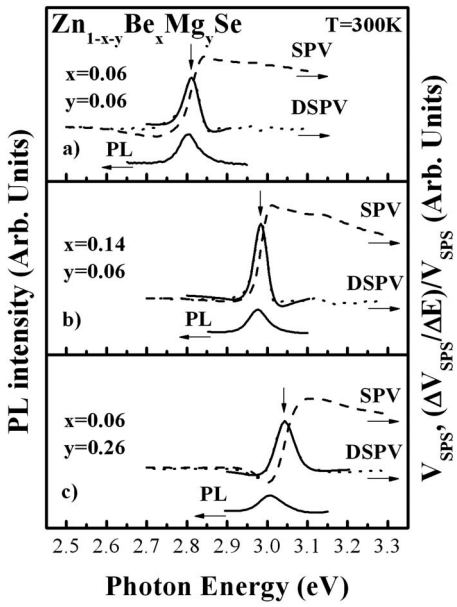

FIG. 5. Room temperature experimental SPS and PL spectra as well as $(\Delta V_{SPS}/\Delta E)/V_{SPS}$ for $Zn_{1-x-y}Be_xMg_ySe$ with different x and y content: (a) $x=0.06$ and $y=0.06$, (b) $x=0.14$ and $y=0.06$, and (c) $x=0.06$ and $y=0.26$, respectively. The arrows show the position of the band-edge excitonic features obtained from DSPV by least-square fits to the first-derivative Lorentzian-lineshape function (solid line).

TABLE I. Room temperature values of the excitonic transition energies obtained from SPS and peak positions of PL spectra for $Zn_{1-x-y}Be_xMg_ySe$ mixed crystals. The parameters for ZB-$Zn_{0.81}Be_{0.04}Mg_{0.15}Se$, ZB-$Zn_{0.96}Be_{0.04}Se$, and ZB-$Zn_{0.93}Mg_{0.07}Se$ at 15 K and room temperature are included for comparison.

Samples	Temperature	E_{SPS} (E_{CER}) (eV)	E_{PL} (eV)	ΔE (meV)
$Zn_{0.88}Be_{0.06}Mg_{0.06}Se$ [a]	300	2.816	2.809	7
$Zn_{0.80}Be_{0.14}Mg_{0.06}Se$ [a]	300	2.987	2.975	12
$Zn_{0.68}Be_{0.06}Mg_{0.26}Se$ [a]	300	3.040	3.011	29
ZB-$Zn_{0.81}Be_{0.04}Mg_{0.15}Se$ [b]	15	3.001	2.986	15
	300	2.886	2.873	13
ZB-$Zn_{0.96}Be_{0.04}Se$ [c]	15	2.901	2.892	9
	300	2.790	2.784	6
ZB-$Zn_{0.93}Mg_{0.07}Se$ [c]	15	2.877	2.862	15
	300	2.765	2.756	9

[a]Present work (SPS and PL).
[b]Reference 24 (CER and PL).
[c]Reference 27 (CER and PL).

where α is the absorption coefficient. The obtained curves are displayed by the dotted lines in Fig. 5. These data were fitted to the first derivative of a Lorentzian lineshape, which is appropriate for excitonic transitions,[22,23] and they are drawn with the solid lines in Fig. 5. The obtained energies are indicated by arrows. As can be seen in Fig. 5, for $Zn_{0.88}Be_{0.06}Mg_{0.06}Se$, the excitonic transition energy obtained from SPS measurements is several meV higher than the peak positions of the band-edge exciton features in the PL spectra. For higher Be and Mg contents, the difference between exciton energy determined from SPV and PL spectra become noticeably larger. It should be noted here that such lower-energy-side shift of PL excitonic feature in comparison with the values determined from SPS and contactless electroreflectance (CER) measurements was revealed for II–VI mixed crystals.[17,24] The excitonic transition energies obtained from SPS and the excitonic peak positions in PL spectra are listed in Table I. Our measurements indicated a much faster rate of band gap increase of about 21 meV/mol % for Be in comparing to 11 meV/mol % for Mg. It is also observed that the DAP feature also decreases with the increase in Be and Mg content. In the case of increasing Mg, the decrease in the DAP feature is much more pronounced than that of Be.

The temperature variations of the experimental values of the band-edge excitonic peak positions in the PL spectra with representative error bars for the three investigated $Zn_{1-x-y}Be_xMg_ySe$ mixed crystals are presented in Fig. 6. The full curves in Fig. 6 are least-squares fits to the Varshni semiempirical relationship as given by[25]

$$E(T) = E(0) - \frac{\alpha T^2}{(\beta + T)}, \tag{1}$$

where $E(0)$ is the energy at 0 K and α and β are constants. The constant α is related to the electron (exciton)-average phonon interaction and β is closely related to the Debye temperature.[25] The values obtained for $E(0)$, α, and β are listed in Table II. For comparison, the parameters for the near-band-edge transition energy of ZB-ZnSe,[26] ZB-$Zn_{0.81}Be_{0.04}Mg_{0.15}Se$,[24] ZB-$Zn_{0.96}Be_{0.04}Se$,[27] ZB-$Zn_{0.93}Mg_{0.07}Se$ (Ref. 27) obtained using contactless electroreflectance measurements are also listed in Table II.

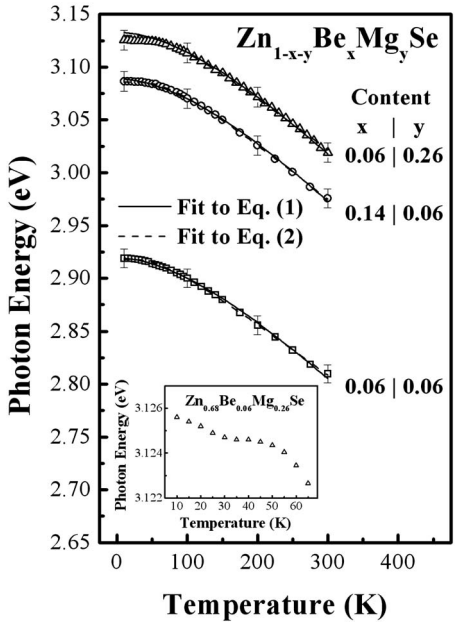

FIG. 6. Temperature variation of the experimental values of energy of the band-edge excitonic line with representative error bars for $Zn_{1-x-y}Be_xMg_ySe$ mixed crystal with different Be and Mg content. The full curves are least-squares fits to Eq. (1) and the dotted lines are least-squares fits to Eq. (2). The inset shows the low temperature region for $Zn_{0.68}Be_{0.06}Mg_{0.26}Se$.

The temperature dependence of the band-edge excitonic transition energies can also be described by a Bose–Einstein-type expression[28]

$$E(T) = E(0) - 2a_B/[\exp(\Theta_B/T) - 1], \tag{2}$$

where $E(0)$ is the energy at 0 K, a_B represents the strength of the electron (exciton)-average phonon interaction, and Θ_B corresponds to the average phonon temperature. Shown by the dotted lines in Fig. 6 is a least-squares fit to Eq. (2). The obtained values for the fitting parameters are also presented in Table II, together with that of the parameters for the near-band-edge transition energy obtained using contactless electroreflectance measurements of ZB-ZnSe,[26] ZB-$Zn_{0.81}Be_{0.04}Mg_{0.15}Se$,[24] ZB-$Zn_{0.96}Be_{0.04}Se$,[27] and ZB-$Zn_{0.93}Mg_{0.07}Se$ (Ref. 27) for comparison.

Taking into account the high-temperature limit of both expressions, the parameter α in Eq. (1) can be related to a_B and Θ_B in Eq. (2) that yields $\alpha = 2a_B/\Theta_B$. Comparison of the values presented in Table II show that this relation is indeed satisfied. From Eq. (2), it is easy to show that the high-temperature limit of the slope of $E(T)$ versus T curve approaches the value of $-2a_B/\Theta_B$. The calculated values of $-2a_B/\Theta_B$ for the band-edge exciton transition X for $Zn_{1-x-y}Be_xMg_ySe$ mixed crystals agrees well with the value of dE_X/dT as obtained from the linear extrapolation of the high-temperature (200–300 K) PL experimental data.

The temperature behavior of the PL excitonic line corresponding to the highest energy in the emission spectra for $Zn_{1-x-y}Be_xMg_ySe$ mixed crystals is different for samples with low and higher magnesium content. For $Zn_{0.88}Be_{0.06}Mg_{0.06}Se$, the exciton emission line monotoni-

TABLE II. Values of Varshni and Bose–Einstein function fitting parameters describing the temperature dependence of the excitonic transition energies of $Zn_{1-x-y}Be_xMg_ySe$ mixed crystals. The parameters for ZB-ZnSe, ZB-$Zn_{0.81}Be_{0.04}Mg_{0.15}Se$, ZB-$Zn_{0.96}Be_{0.04}Se$, and ZB-$Zn_{0.93}Mg_{0.07}Se$ are included for comparison.

Samples	Feature	$E(0)$ (eV)	α (meV/K)	β (K)	a_B (meV)	Θ_B (K)
$Zn_{0.88}Be_{0.06}Mg_{0.06}Se$ [a]	X	2.918 ± 0.003	0.74 ± 0.03	295 ± 20	43 ± 4	175 ± 30
$Zn_{0.80}Be_{0.14}Mg_{0.06}Se$ [a]	X	3.089 ± 0.003	0.78 ± 0.03	303 ± 20	50 ± 4	196 ± 30
$Zn_{0.68}Be_{0.06}Mg_{0.26}Se$ [a]	X	3.131 ± 0.003	0.79 ± 0.03	308 ± 20	53 ± 4	199 ± 30
ZB-$Zn_{0.81}Be_{0.04}Mg_{0.15}Se$ [b]	E_0	3.001 ± 0.003	0.79 ± 0.03	300 ± 20	59 ± 4	210 ± 30
ZB-ZnSe[c]	E_0	2.800 ± 0.003	0.73 ± 0.04	295 ± 35	73 ± 4	260 ± 30
ZB-$Zn_{0.96}Be_{0.04}Se$ [d]	E_0	2.903 ± 0.003	0.72 ± 0.03	281 ± 20	52 ± 4	200 ± 30
ZB-$Zn_{0.93}Mg_{0.07}Se$ [d]	E_0	2.877 ± 0.003	0.73 ± 0.03	285 ± 20	54 ± 4	205 ± 30

[a]Present work (PL).
[b]Reference 24 (electromodulation).
[c]Reference 26 (CER).
[d]Reference 27 (CER).

cally shifts toward lower photon energy with the increase in temperature following the temperature variation of the band-gap energy. For low Mg content in $Zn_{1-x-y}Be_xMg_ySe$ mixed crystals, the temperature dependence of the discussed PL line can be well described with the Varshni formula and Bose–Einstein-type expression in the entire measured temperature range similar to pure ZnSe and $Zn_{1-x}Mg_xSe$ with lower than about 0.10 of magnesium content.[29] For higher Mg concentrations, however, the temperature behavior of excitonic line is quite different at low temperatures where some deviation from the described relations starts to appear. For $Zn_{0.68}Be_{0.06}Mg_{0.26}Se$ sample (Fig. 6), in the temperature range between 10 and 30 K, the maximum of this PL line shifts toward lower photon energies as the temperature increases. With a further increase in temperature from 30 to about 60 K the energetic position of the maximum of this emission line became almost independent on temperature or even slightly shifts toward higher energies with the temperature rise. Above 60 K, the normal shift toward lower energies with increasing temperature is observed in accordance with the temperature dependence of the energy gap reduction. The Be content influence on the temperature behavior of excitonic peak position in PL spectra was not observed mostly because of small Be content in $Zn_{1-x-y}Be_xMg_ySe$ ($x \leq 0.15$). The atypical nonmonotonic S-shape type temperature behavior of the discussed above excitonic feature of PL spectra for the investigated crystals is the characteristic feature of emission due to the radiative recombination of localized excitons, and it was observed in $Zn_{1-x}Mg_xSe$,[29] $Cd_{1-x}Mg_xSe$,[29] $Zn_{1-x-y}Cd_xMg_ySe$,[30] $Cd_{1-x}Be_xSe$,[31] $ZnSe_{1-x}Te_x$,[32] and $Al_xGa_{1-x}N$.[33] Such exciton localization is due to spatial potential fluctuations being a consequence of the statistical fluctuations of concentrations of particular components in the mixed crystals. It has been shown[34] that the existence of such random potential fluctuations leads to variation of the particular energy levels in the mixed crystals. As a result, the smearing of the band edges takes place leading to the fluctuations of the band-gap energy and to formation of band tails where the localization of excitons and carriers can take place. The effective localization of photoexcited carriers appeared when the average density of localized states is larger than the density of states due to impurities and native defects.[34,35] The shift of the excitonic feature in reflectivity spectrum as compared to that in PL spectrum observed for $Zn_{1-x}Mg_xSe$ crystals with high Mg content supports the excitonic localization process.[36]

The temperature dependence of the linewidth $\Gamma(T)$ of the band-edge exciton features obtained by PL measurements for $Zn_{1-x-y}Be_xMg_ySe$ are displayed in Fig. 7. Initially, $\Gamma(T)$ linearly enlarges with increasing temperature, but it begins to be superlinear starting from about 150 K. The temperature dependence of the linewidth of excitonic transitions of semiconductors can be expressed as[37]

$$\Gamma(T) = \Gamma(0) + \gamma_{AC}T + \frac{\Gamma_{LO}}{[\exp(\Theta_{LO}/T) - 1]}, \quad (3)$$

where $\Gamma(0)$ represents the broadening invoked from temperature-independent mechanisms, such as electron-

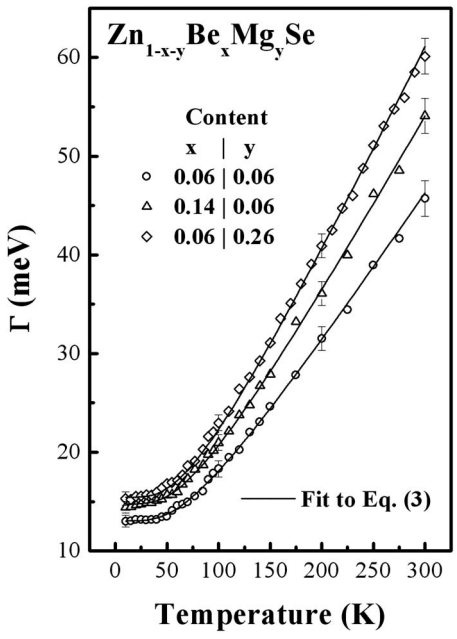

FIG. 7. Experimental data of the temperature dependence of the linewidth $\Gamma(T)$ of the excitonic features with representative error bars obtained from PL measurements for $Zn_{1-x-y}Be_xMg_ySe$ mixed crystal with different Be and Mg content. The full curves are least-squares fits to Eq. (3).

TABLE III. Values of the parameters that describe the temperature dependence of the broadening function $\Gamma(T)$ for edge excitonic transition of $Zn_{1-x-y}Be_xMg_ySe$ mixed crystal samples. The parameters for ZB-ZnSe, ZB-$Zn_{0.96}Be_{0.04}Se$, and ZB-$Zn_{0.93}Mg_{0.07}Se$ are included for comparison.

Samples	Feature	$\Gamma(0)$ (meV)	Γ_{LO} (meV)	Θ_{LO} (K)	γ_{AC} (μeV/K)
$Zn_{0.88}Be_{0.06}Mg_{0.06}Se$ [a]	X	13.0 ± 2.0	31 ± 6	250 ± 75	3 ± 1
$Zn_{0.80}Be_{0.14}Mg_{0.06}Se$ [a]	X	14.7 ± 2.0	36 ± 6	260 ± 75	3 ± 1
$Zn_{0.68}Be_{0.06}Mg_{0.26}Se$ [a]	X	15.4 ± 2.2	42 ± 7	265 ± 75	3 ± 1
ZB-ZnSe[b]	E_0	6.5 ± 2.5	24 ± 8	360 ± 80	2[d]
ZB-$Zn_{0.96}Be_{0.04}Se$ [c]	E_0	13.7 ± 2.0	47 ± 8	250 ± 80	3 ± 1
ZB-$Zn_{0.93}Mg_{0.07}Se$ [c]	E_0	16.9 ± 2.0	50 ± 8	260 ± 80	3 ± 1

[a]Present work (PL).
[b]Reference 26 (CER).
[c]Reference 27 (CER).
[d]A fixed parameter.

electron interaction, impurity, dislocation, and alloy scattering, whereas the second term corresponds to lifetime broadening due to the exciton-acoustical phonon interaction with γ_{AC} being the acoustical phonon coupling constant. The third term is caused by the exciton-LO phonon (Fröhlich) interaction. The quantity Γ_{LO} represents the strength of the exciton-LO phonon coupling while Θ_{LO} is the LO-phonon temperature.[28,38] The full curves in Fig. 7 are least-squares fits of experimental data to Eq. (3) to evaluate $\Gamma(0)$, Γ_{LO}, Θ_{LO}, and γ_{AC} for the band-edge exciton feature of the investigated samples. The obtained values of $\Gamma(0)$, Γ_{LO}, Θ_{LO} and γ_{AC} are listed in Table III. For comparison, the values of $\Gamma(0)$, Γ_{LO}, Θ_{LO}, and γ_{AC} for ZB-ZnSe,[26] ZB-$Zn_{0.96}Be_{0.04}Se$,[27] and ZB-$Zn_{0.93}Mg_{0.07}Se$ [27] obtained from contactless electroreflectance measurements are also included in Table III. As shown in Table III, the value of $\Gamma(0)$ for $Zn_{1-x-y}Be_xMg_ySe$ samples is much larger than those of the previously reported Be/Mg-free sample, such as ZnSe,[26] mainly due to the poorer crystalline quality of the Be/Mg incorporated samples. The fitted value of Γ_{LO} for $Zn_{1-x-y}Be_xMg_ySe$ samples is larger than those of Be/Mg-free samples. The value of Γ_{LO} in $Zn_{1-x-y}Be_xMg_ySe$ is influenced by the alloy disorder. It is also presumably related to the higher effective longitudinal optical phonon energy of the Be/Mg containing samples. In addition, it is possible that a larger deformation potential interaction, which may account for a significant fraction of Γ_{LO} in addition to the Fröhlich interaction, is responsible for the larger Γ_{LO} for $Zn_{1-x-y}Be_xMg_ySe$ mixed crystals.

IV. SUMMARY

In summary, the investigations of the near-band-edge transitions of high-pressure Bridgman-grown $Zn_{1-x-y}Be_xMg_ySe$ mixed crystal samples have been carried out by temperature-dependent PL in the range of 10 to 300 K and room temperature SPS measurements. PL spectra at low temperatures consist of an exciton line, a broader emission band due to recombination of shallow DAPs, and a broad band related to recombination through DL defects. Interband transitions, originating from the band edge have been observed in the SPV spectra. The anomalous S-shape temperature dependence of the exciton PL peak is observed for $Zn_{1-x-y}Be_xMg_ySe$ crystals with high Mg content ($y=0.26$). The results of detailed investigations of temperature dependence of luminescence can be explained as due to localization of excited carriers caused by statistical fluctuations of local composition. The peak positions of the excitonic emission lines in PL spectra correspond quite well to the energies of the fundamental transitions determined from SPV measurements. Our results indicated a much faster rate of band gap increase of about 21 meV/mol % for Be in comparing to 11 meV/mol % for Mg. The fitted value of Γ_{LO} for $Zn_{1-x-y}Be_xMg_ySe$ samples is larger than those of Be/Mg-free samples. A larger deformation potential interaction, which may account for a significant fraction of Γ_{LO} in addition to the Fröhlich interaction, is responsible for the larger Γ_{LO} for $Zn_{1-x-y}Be_xMg_ySe$ mixed crystals.

ACKNOWLEDGMENTS

The authors acknowledge the supports of National Science Council of Taiwan under Project No. NSC 96-2221-011-030 and NTUST-NCU International Joint Research Project No. RP07-02. This work was also supported in part by the Committee for Scientific Research of Poland under Grant No. 1 P03B 092 27 (realized in 2004–2007).

[1]S. O. Ferreira, H. Sitter, W. Faschinger, R. Krump, and G. Brunthaler, J. Cryst. Growth **146**, 418 (1995).
[2]S. O. Ferreira, H. Sitter, R. Krump, W. Faschinger, G. Brunthaler, and J. Sadowski, Semicond. Sci. Technol. **10**, 489 (1995).
[3]C. Vèrié, in *Semiconductors Heteroepitaxy*, edited by B. Gil and R. L. Aulombvard (World Scientific, Singapore, 1995), Vol. 1, p. 73.
[4]A. A. Wronkowska, A. Wronkowski, F. Firszt, S. Łęgowski, H. Męczyńska, A. Marasek, and W. Paszkowicz, Phys. Status Solidi C **1**, 641 (2004).
[5]F. Vigue, E. Tournie, and J. P. Faurie, IEEE J. Quantum Electron. **37**, 1146 (2001).
[6]F. Vigue, E. Tournie, J. P. Faurie, E. Monroy, F. Calle, and E. Muñoz, Appl. Phys. Lett. **78**, 4190 (2001).
[7]A. Nurmikko and R. L. Gunshor, Semicond. Sci. Technol. **12**, 1337 (1997).
[8]T. Nakamura, K Katayama, H. Mori, and S. Fujiwara, Phys. Status Solidi B **241**, 2659 (2004).
[9]M. Adachi, K. Ando, T. Abe, N. Inoue, A. Urata, S. Tsutsumi, Y. Hashimoto, H. Kasada, K. Katayama, and T. Nakamura, Phys. Status Solidi B **243**, 943 (2006).
[10]T. Nakamura, Electr. Eng. Jpn. **154**, 42 (2006).
[11]W. Paszkowicz, K. Godwod, J. Domagała, F. Firszt, J. Szatkowski, H. Męczyńska, S. Łęgowski, and M. Marczak, Solid State Commun. **107**, 735 (1998).

[12]F. Firszt, A. A. Wronkowska, A. Wronkowski, S. Łęgowski, A. Marasek, H. Męczyńska, M. Pawlak, W. Paszkowicz, K. Strzałkowski, and A. J. Zakrzewski, Cryst. Res. Technol. **40**, 386 (2005).
[13]Y. S. Huang, L. Malikova, F. H. Pollak, H. Shen, P. Pamulapati, and P. Newman, Appl. Phys. Lett. **77**, 37 (2000).
[14]L. Kronik and Y. Shapira, Surf. Sci. Rep. **37**, 1 (1999).
[15]F. Firszt, Semicond. Sci. Technol. **8**, 712 (1993).
[16]A. M. Mintairov, S. Raymond, J. L. Merz, F. C. Peiris, S. Lee, U. Bindley, J. K. Furdyna, V. G. Melehin, and K. Sadchikov, Semiconductors **33**, 1021 (1999).
[17]J. Z. Wang, P. J. Huang, H. P. Hsu, Y. S. Huang, F. Firszt, S. Łęgowski, H. Męczyńska, A. Marasek, and K. K. Tiong, J. Appl. Phys. **101**, 103539 (2007).
[18]J. Z. Wang, P. J. Huang, Y. S. Huang, F. Firszt, S. Łęgowski, H. Męczyńska, A. Marasek, and K. K. Tiong, J. Phys.: Condens. Matter **19**, 096216 (2007).
[19]F. Plazaola, K. Saarinen, L. Dobrzyński, H. Reniewicz, F. Firszt, J. Szatkowski, H. Męczyńska, S. Łęgowski, and S. Chabik, J. Appl. Phys. **88**, 1325 (2000).
[20]F. Plazaola, J. Flyktman, K. Saarinen, L. Dobrzyński, F. Firszt, S. Łęgowski, J. H. Męczyńska, and H. Reniewicz, J. Appl. Phys. **91**, 1647 (2003).
[21]L. Kronik and Y. Shapira, Surf. Interface Anal. **31**, 954 (2001).
[22]F. H. Pollak and H. Shen, Mater. Sci. Eng., R. **10**, XV (1993).
[23]Y. S. Huang and F. H. Pollak, Phys. Status Solidi A **202**, 1193 (2005).
[24]P. J. Huang, H. P. Hsu, Y. S. Huang, F. Firszt, S. Łęgowski, H. Męczyńska, A. Marasek, and K. K. Tiong, J. Appl. Phys. **102**, 083515 (2007).
[25]Y. P. Varshni, Physica (Utrecht) **34**, 149 (1967).
[26]L. Malikova, W. Krystek, F. H. Pollak, N. Dai, A. Cavus, and M. C. Tamargo, Phys. Rev. B **54**, 1819 (1996).
[27]H. P. Hsu, P. J. Huang, C. T. Huang, Y. S. Huang, F. Firszt, S. Łęgowski, H. Męczyńska, K. Strzałkowski, A. Marasek, and K. K. Tiong, J. Appl. Phys. **103**, 013501 (2008).
[28]S. Logothetidis, M. Cardona, P. Lautenschlager, and M. Garriga, Phys. Rev. B **34**, 2458 (1986).
[29]F. Firszt, H. Męczyńska, S. Łęgowski, and W. Paszkowicz, J. Alloys Compd. **371**, 107 (2004).
[30]X. Zhou, Y. Gu, Igor L. Kuskovsky, G. F. Neumark, L. Zeng, and M. Tamargo, J. Appl. Phys. **94**, 7136 (2003).
[31]O. Maksimov, M. Muñoz, and M. C. Tamargo, Microelectron. J. **37**, 19 (2006).
[32]A. Naumov, H. Stanzl, K. Wolf, S. Lankes, and W. Gebhardt, J. Appl. Phys. **74**, 6178 (1993).
[33]J. Li, K. B. Nam, J. Y. Lin, and H. X. Jiang, Appl. Phys. Lett. **79**, 3245 (2001).
[34]S. Permogorov, A. Reznitskii, S. Verbin, G. O. Müller, P. Flögel, and M. Nikiforova, Phys. Status Solidi B **113**, 589 (1982).
[35]S. Permogorov and A. Reznitsky, J. Lumin. **52**, 201 (1992).
[36]M. Wörz, E. Griebl, Th. Reisinger, R. Flierl, B. Haserer, T. Semmler, T. Frey, and W. Gebhardt, Phys. Status Solidi B **202**, 805 (1997).
[37]J. Lee, E. Koteles, and M. O. Vassell, Phys. Rev. B **33**, 5512 (1986).
[38]P. Lautenschlager, M. Garriga, S. Logothetidis, and M. Cardona, Phys. Rev. B **35**, 9174 (1987).